Reviews in Mineralogy & Geochemistry
Vol. 83 pp. 153–182, 2017

Electron Microprobe Petrochronology

Michael L. Williams, Michael J. Jercinovic

Department of Geosciences
University of Massachusetts
Amherst MA 01003
USA

mlw@geo.umass.edu

mjj@geo.umass.edu

Kevin H. Mahan

Department of Geological Sciences
University of Colorado
Boulder, CO 80302
USA

mahank@colorado.edu

Gregory Dumond

Department of Geosciences
University of Arkansas
Fayetteville, AR 72701
USA

gdumond@uark.edu

INTRODUCTION

The term petrochronology has increasingly appeared in publications and presentations over the past decade. The term has been defined in a somewhat narrow sense as "the interpretation of isotopic dates in the light of complementary elemental or isotopic information from the same mineral(s)" (Kylander-Clark et al. 2013). Although complementary isotopic and elementary information are certainly a central and critical part of most, if not all, petrochronology studies, the range of recent studies that might use the term covers a much broader scope. The term "petrochronology" might alternatively be defined as the detailed incorporation of chronometer phases into the petrologic (and tectonic) evolution of their host rocks, in order to place direct age constraints on petrologic and structural processes. As noted by Kylander-Clark et al. (2013), the linkage between geochronology and petrology can involve a variety of data including mineral textures and fabrics, the distribution of mineral modes or volume proportions, compositional zoning, mineral inclusion relationships, and certainly major element, trace element, and isotopic composition of the chronometer and all other phases.

Electron probe micro-analysis (EPMA) has a central and critical role to play in establishing the linkage between chronometer phases and their host assemblage. The basic instrument is an electron microscope which can be used in either scanning or fixed beam modes, with integrated wavelength dispersive spectrometers (WDS), energy dispersive spectrometers (EDS), electron detectors (to image secondary and backscattered signals) a light optical system, and optionally cathodoluminescence (CL) detection. The electron microprobe is used to investigate the distribution, composition, and compositional zonation of all mineral phases, the

1529-6466/17/0083-0005$05.00 (print)
1943-2666/17/0083-0005$05.00 (online)
http://dx.doi.org/10.2138/rmg.2017.83.5

data that underpin thermobarometric analysis and modeling of *P–T* histories. The microprobe, with μm-scale spatial resolution, can also characterize compositional zonation in very small accessory phases including monazite, xenotime, zircon, allanite, titanite, apatite, and others. This, as discussed below, can be a critical step in linking geochronology to petrology. Finally, in many circumstances, the microprobe can be used to determine or constrain the age of domains within certain chronometers, especially monazite and xenotime. Where the compositional domains are small (<5 μm), the microprobe may be the only feasible tool that can constrain the age. Narrow rim domains are commonly key constraints on the petro-tectonic history.

This chapter is focused on the role of EPMA in petrochronological studies. The early parts of the chapter highlight analytical considerations in using the electron microprobe: first, for compositional characterization and for establishing the linkage between chronometer phases and the petro-tectonic history, and second, for precise trace element analysis and dating. Although the process is relatively straightforward, special analytical methods must be adopted for high-precision trace element analysis by electron microprobe. The later parts of the chapter provide examples and illustrations of the different roles that the electron microprobe can play in petrochronological studies. Many of the examples, and much of the recent research, concern monazite and xenotime in deformed and metamorphosed rocks. Although zircon has been widely used to constrain age or provenance, and more rarely metamorphic history, monazite and xenotime can record, with high fidelity, multiple stages in the igneous and metamorphic history and can also provide some key constraints on the deformational history. Finally, it should be noted that neither the techniques nor the electron microprobe instrument itself have reached their ultimate potential for petrochronological analysis. We hope to shine some light on future directions and challenges that suggest the ability to more efficiently extract, and to more tightly constrain, the *P–T*–time–deformation history of rocks.

REACTION DATING

One of the major goals of igneous or metamorphic analysis is determining the sequence of minerals or mineral assemblages that were present during the evolution of the rocks of interest, and ultimately interpreting the sequence of chemical reactions that relate the minerals or assemblages. The characterization of mineral assemblages and reactions, based on petrographic, petrologic, and microstructural analysis allows the construction of *P–T–t* (±*D* = deformation) histories that are central to most petrologic investigations. Although in some previous studies, workers have used resetting of geochronometers during metamorphism as a means to constrain the "age of metamorphism", the very sluggish rate of diffusion in high-temperature chronometers such as zircon, monazite, or xenotime (Cherniak et al. 2004; Cherniak and Pyle 2008; Cherniak 2010), make resetting generally unlikely. Instead, new mineral grains (neocrystals), or new domains within chronometer minerals, probably grow during the reaction history. This is particularly true of monazite, which can serve as a source or sink of a wide variety of elements, including Rare Earths, actinides, and others, that are minor and trace elements in most silicates. As such, the essence of petrochronology involves integrating trace elements and trace-element-bearing chronometer phases into the silicate reaction history. Trace element partitioning may place additional constraints on the metamorphic equilibria (Hickmott and Spear 1992; Bea et al. 1997; Pyle and Spear 1999; Yang et al. 1999; Spear and Pyle 2002), and in the present context, dating specific generations of chronometer phases that have been associated with a particular reaction allows a date to be directly associated with a reaction. This process could be described as "reaction dating" and we note that it is increasingly becoming the focus of many researchers around the world (for example Larson et al. 2011; Dumond et al. 2015; Regis et al. 2016; and many others). Focusing on the term, "reaction dating" deemphasizes the goal of "dating metamorphism" and instead, emphasizes the goal of dating or constraining as many prograde and retrograde reactions as possible, in order to characterize the timing and hopefully duration of metamorphic or igneous events.

Most of the examples and illustrations in this chapter focus on petrochronology involving monazite and to a lesser extent xenotime and zircon. For many reasons, monazite may be the ideal chronometer for EPMA petrochronology. First, monazite has a wide stability field from diagenesis to high-grade metamorphism, and it occurs in a range of metamorphic and igneous rock compositions (Overstreet 1967; Williams et al. 2007; Catlos 2013). Further, its broad compositional range implies that monazite can, to some degree, participate in a variety of silicate reactions, serving as a source or sink of minor components that are also present in the silicate minerals. There are many examples of monazite or xenotime reacting to (or from) other phosphate or REE-bearing minerals (Finger et al. 1998; Janots et al. 2008; Budzyn et al. 2011), but as discussed below, monazite compositions can also be modified during many silicate reactions because of minor components either liberated or consumed during the reaction(s). Finally, monazite is particularly amenable to electron microprobe analysis. In addition to U, Th, and Pb, many components, including light REEs and actinides, are abundant enough to be analyzed by EPMA. The current analytical protocol at the University of Massachusetts includes 25 elements in a standard monazite analysis. Many other minerals can provide key petrochronological data including apatite, allanite, titanite, thorite, uraninite, and others (see also Vance et al. 2003). The methods described below are applicable to varying degrees to all of these phases. Examples of some representative studies are highlighted, but many other examples could certainly be included.

Monazite has been an important geologic chronometer since the classic study of Parrish (1990). However, starting in the late 1990s, a large number of studies documented multiple generations of metamorphic monazite (and xenotime) and to varying degrees attempted to integrate monazite or xenotime generations with silicate reactions. They illustrate the steadily evolving logic used to correlate monazite generations and silicate reactions and assemblages. Early studies tended to focus on Y-concentration because of the inverse relationship with garnet abundance (Pyle and Spear 1999, 2003; Wing et al. 2003; Foster et al. 2004; Gibson et al. 2004; Berger et al. 2005; Kohn et al. 2005; McFarlane et al. 2005; Yang and Pattison 2006). Along with heavy Rare Earth Elements, Y is strongly partitioned into garnet, and as such, Y in monazite (and the overall abundance of xenotime) typically decreases during garnet growth and increases on garnet break-down. This Y–garnet–monazite–xenotime connection is still one of the most powerful and widely used petrochronological tools, especially for microprobe-based studies.

More recently, workers have considered other trace components and proposed increasingly more specific reactions and mechanisms linking accessory phases with silicate assemblages (i.e., Rubatto et al. 2006; Buick et al. 2010; Dumond et al. 2015; Regis et al. 2016; Rocha et al. in press). In addition, new experimental data and studies of well-constrained natural assemblages have provided constraints on partitioning between accessory phases and silicate assemblages and melts (Hermann and Rubatto 2003; Krenn and Finger 2004; Rubatto and Hermann 2007; Stepanov et al. 2012), updating and expanding the classic work of Bea and coworkers (Bea et al. 1994; Bea and Montero 1999). One ultimate goal is to better constrain the thermodynamic properties of accessory phases such that the accessory chronometers can be incorporated into phase diagrams, particularly isochemical phase diagram models (see below). Several important steps have been made in modeling monazite, xenotime, and zircon abundance and composition in metamorphic rocks and in melt–silicate systems (Kelsey et al. 2008; Spear 2010; Spear and Pyle 2010; Kelsey and Powell 2011).

COMPOSITIONAL MAPPING, TRACE ELEMENT ANALYSIS, AND DATING BY ELECTRON MICROPROBE

Compositional mapping for petrochronology

Compositional maps have been used for many years to explore zoning in single minerals (Tracy 1982; c.f. Kohn 2013). Early maps made by contouring point analyses were time consuming and generally of low resolution. Modern maps made by rastering the electron microprobe (beam or stage) or by mosaicking a grid of smaller SEM images are simple and

efficient to collect. Resolution can be as high as 1 μm per pixel (or better), although time constraints may limit the resolution for larger maps.

Full-thin-section or large-area compositional maps are much less common in the literature, but can be invaluable for petrochronological analysis (Fig. 1). Maps of major element abundances, commonly Mg, Ca, K etc. can show the distribution of major phases and also significant compositional zoning within the larger minerals. Maps of selected elements (Ce for monazite, Y for xenotime, Zr for zircon) can be used to locate accessory chronometer phases (see also Williams et al. 2006; Larson et al. 2011). Depending on the number of elements required and number of available spectrometers or compositional channels, multiple mapping acquisitions of the same area may be necessary in order to identify and characterize the major and accessory phases of interest. Background maps (maps collected in a background position for the desired element) or calculated backgrounds based on mean atomic number (Donovan et al. 2016) can be subtracted from peak-position compositional maps in order to perform a background correction. Also, peak pixel values can be calibrated in order to constrain phase compositions (see also Kohn and Spear 2000; Clarke et al. 2001; De Andrade et al. 2006), and image math can be used to calculate hybrid maps such as age maps (Goncalves et al. 2005). Commonly, a single set of maps can be used to successfully identify the major phases and to locate and evaluate the chronometer phases. Other instruments (and methods) besides electron microprobe WDS mapping are available for large-area compositional mapping, including scanning electron microscopy (SEM) with EDS (sometimes also WDS) and electron backscatter diffraction (EDS and EBSD) capabilities, and the related electron beam techniques offered by quantitative evaluation of minerals by scanning electron microscopy (QEMSCAN), and mineral liberation analysis (MLA). QEMSCAN in particular is capable of efficiently capturing compositional information from minerals in large-area maps, although these instruments, to date, have mainly been used in economic geology applications.

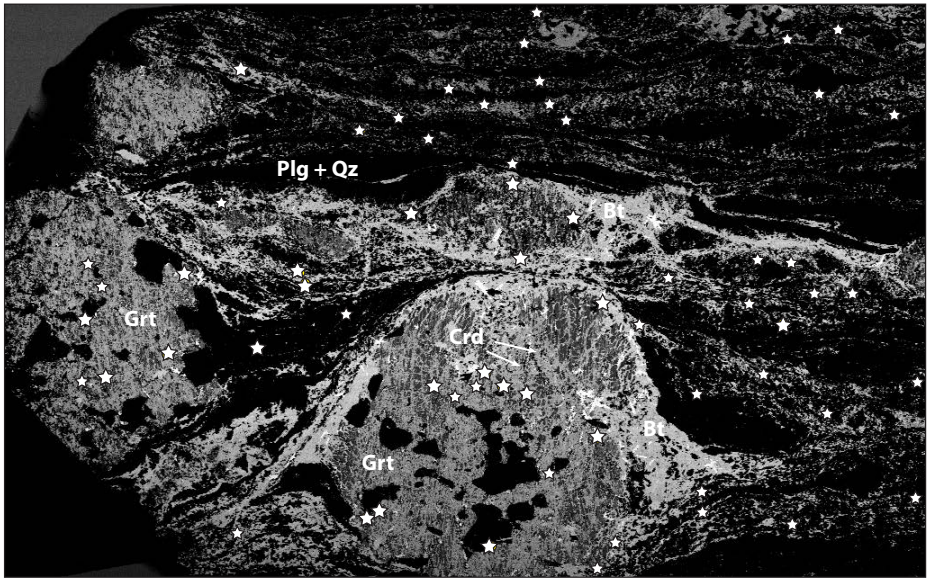

Figure 1. Full-thin-section Mg Kα compositional map of sample S32D. Lighter grey tone corresponds to great Mg content. The large central subhedral garnet has been partly replaced by biotite (outside) and cordierite on fractures within the crystal. Abbreviations from Whitney and Evans (2010). White stars show the location of Monazite grains; larger stars are larger grains. The stars represent (i.e., are placed on) high-Ce pixels (or clusters of pixels) on the full-section map. The map was run at 300 nA, 25 ms/pixel with a 35 μm step size and 25–30 μm beam. Modified from Mahan et al. (2006).

Large-area maps showing the location of chronometer phases are, in themselves, useful tools for illuminating the petrogenesis of the major and the accessory phases. For example xenotime grains specifically situated around the rim of garnet crystals commonly represent late-stage xenotime growth during garnet resorption (Fig. 2). Zircon in leucosome domains can represent zircon formed during melt crystallization (Flowers et al. 2006a). These maps are particularly useful when they are generated early in the petrographic/petrologic analysis cycle rather than later after the petrographic analysis and interpretation has been completed.

High-resolution (small-area) maps of chronometer phases, including WDS, cathodoluminescence, backscattered electron, etc., have been used extensively to characterize zoning in chronometer phases in order to plan a strategy for dating, and to aid in interpreting geochronologic results (Williams et al. 2006, 2007; Larson et al. 2011; Peterman et al. 2016; and many others). When placed into the context of full-section compositional maps, the high-resolution maps can be an even more powerful tool for petrochronology and reaction dating. One method for integrating the maps involves placing the high-resolution maps around or on the full-section image with links to the actual grain locations (Fig. 3a). This allows the zonation within a high-resolution map to be interpreted in the context of its setting within the thin section. Recent work has shown that even the most subtle compositional zoning in monazite can reflect the local setting in the thin section (i.e., porphyroblast inclusion relations, nearby phases, local structures, fractures). It is particularly important to process the high-resolution compositional maps with the same look-up table such that similar compositions have similar intensities on the images (Williams et al. 2006). One simple technique using Adobe software is summarized in Appendix-1 (deposited with MSA and available from the authors).

The combination of high-resolution and low-resolution (large area) compositional maps allows chronometer phases to be integrated into the petrographic analysis process. In the case of monazite, zircon, or xenotime, it is commonly possible to identify several key generations of the chronometer phase(s) and to relate the generations, at least in a qualitative way, to the silicate phases/assemblages and to fabric generations. This also changes the nature of the geochronologic analysis strategy. Rather than dating a number of grains and interpreting ages, the analytical strategy involves first, verifying that chronometer populations identified on compositional maps actually represent specific

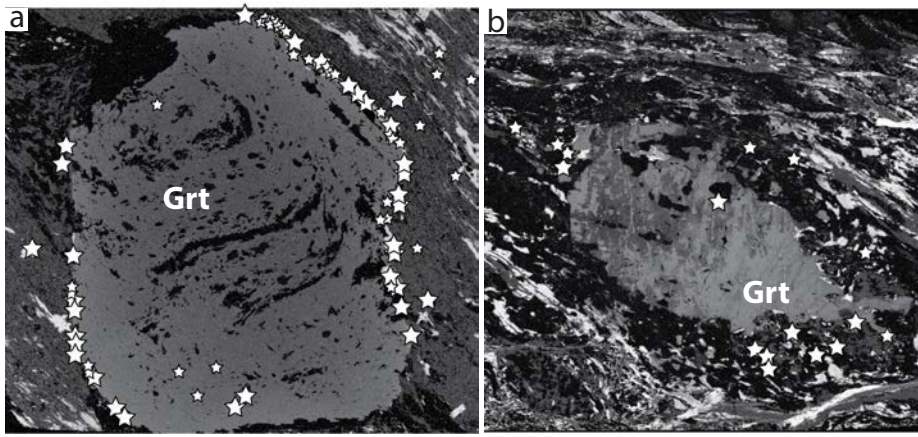

Figure 2. (a) Ca Kα compositional map of garnet from Vermont showing xenotime crystals concentrated on the margin of resorbed garnet. Modified from Gatewood et al. (2015). (b) Mg Ka map showing resorbed garnet from the Park Range, Colorado. Xenotime is concentrated in sinistral strain shadows of the garnet. The xenotime is interpreted to have been stabilized during garnet breakdown and release of Y.

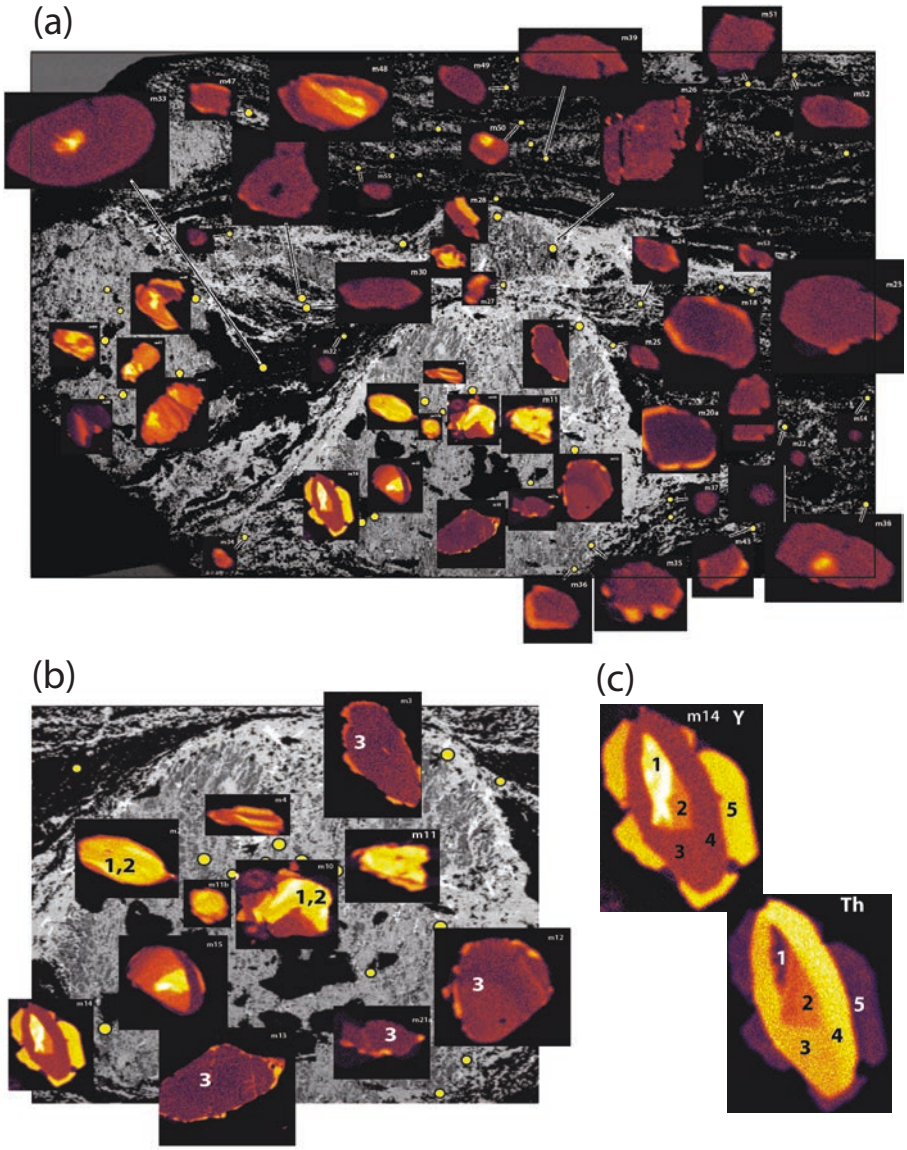

Figure 3. (a) Full-thin-section Mg Kα compositional map of sample S32D (Fig. 1) with superimposed high-resolution Y Lα monazite grain maps. (b) Close-up of central garnet. Note inclusions in inner core contain monazite generations Mz1 and Mz2. Outer inclusions are dominated by generation Mz3. (c) High-resolution Y Lα map of Mz14 showing all five generations of monazite. See text for discussion. Modified from Mahan et al. (2006) and Villa and Williams (2012).

compositional and geochronological populations and second, dating ("sampling") each population in order to constrain the age of the particular assemblages or fabrics.

Trace element maps of silicate phases can add additional insights. Trace-element maps can be acquired by EPMA, and are particularly straightforward in minerals such as garnet and olivine that are stable under high sample current (Spear and Kohn 1996; Pyle and Spear 1999;

Goodrich et al. 2013; Kohn 2013). Trace element mapping has also recently been done by LA-ICP-MS (Kylander-Clark 2017; Lanari and Engi 2017). With several notable exceptions, this is a largely untapped opportunity for relating chronometer phases to silicate assemblages. Pyle and Spear (1999) used high-current mapping of Y in garnet and documented the close coupling between Y in garnet and xenotime in metamorphic rocks over a range of metamorphic grades from garnet nucleation to partial melting. The xenotime–garnet relationships provide insights into parts of the *P–T* history that are not well constrained by the major elements and silicate phases alone; several thermometers have been calibrated for Y partitioning between garnet and xenotime, and the xenotime itself can be dated, commonly by electron probe, in order to place timing constraints on parts of the prograde and retrograde *P–T* path.

It is worth noting that many geochronological studies involve dating a large number of chronometer grains/domains, plotting dates on an "age histogram" and then interpreting populations. This "top-down" approach is useful for detrital mineral analysis, but is less appropriate for analysis of metamorphic or igneous rocks. The "bottom-up" approach (Williams et al. 2006) involves: (1) establishing populations, based on composition and texture; (2) developing hypotheses about chronometer-forming reactions and relative timing; and (3) constraining the age of the populations using the most appropriate analytical technique. For chronometers such as monazite and xenotime, narrow rim domains can be very important for constraining the petrologic history. For these domains, electron microprobe total Pb dating may be the only analytical option.

Trace-element analysis by electron microprobe—analytical considerations

The electron microprobe was initially developed for, and most applications involved, rapid non-destructive major and minor element analysis. However, even during the early development, some workers (e.g., Goldstein and Wood 1966; Goldstein 1967) recognized that the instrumentation had great utility in the trace element realm (below 1 wt.%). In the modern age, where LA-ICP-MS and Ion Microprobe instruments can analyze a broad suite of trace elements with low detection limits (e.g., Kylander-Clark 2017; Schmitt and Vazquez 2017), EPMA still has numerous applications in the measurement of minor and trace components, especially when non-destructive analysis and high spatial resolution are important. Further, during the past several decades, there have been a number of significant improvements in hardware, software, and analytical procedures that have increased EPMA precision and accuracy for trace element analysis.

U–Pb dating (i.e., total-Pb dating) by EPMA is a relatively new application (Parslow et al. 1985; Bowles 1990; Suzuki and Adachi 1991; Asami et al. 1996; Montel et al. 1996; Cocherie et al. 1998; Williams et al. 1999). It is based on the assumption that common Pb is insignificant compared to radiogenic Pb in U- and Th-rich (and Ca-poor) phases like monazite, xenotime, zircon, uraninite, or thorite. As such, accurate measurement of the total amount of Pb, U, and Th can be used to calculate a date from very small domains in the chronometer phases. As noted above, many compositional domains, especially rim domains and core domains, can be extremely small or narrow, but are critical for constraining *P–T* histories. Although Th can be present in monazite at the major or minor element level, U and Pb are almost always trace element measurements whose emission lines lie in a complicated part of the X-ray spectrum, particularly when REEs are present.

One lesson learned over the past decade is that it is not adequate to apply the major element analytical protocol to trace elements and simply increase the current and count time. Every aspect of the analytical routine, from sample (and standard) preparation to data processing, must be specifically designed for the trace elements involved and for the particular application (e.g., Scherrer et al. 2000; Jercinovic et al. 2008). Many aspects of the analytical problems and potential solutions have been described in other publications (Pyle et al. 2002; Williams et al. 2006; Jercinovic and Williams 2005; Jercinovic et al. 2008, 2012; Spear et al. 2009). The following paragraphs summarize some of the most recent improvements and some of the major

Table 1. Analytical Steps in EPMA Geochronology.

	Procedure	Instrument Setup
1	Find the accessory minerals in thin section (monazite, xenotime, zircon, thorite, uraninite, etc.) by full thin section mapping. Ce, Y, Zr, Mg, Ca.	15 kV, 300 nA, 25 ms/pixel, 35 mm beam diameter. 35 mm step, stage raster.
2	Process full section maps to overlay indicator elements on base map (reveals accessory mineral grain locations in relation to microstructure).	15 kV, 200 nA, 80 ms/pixel.
3	Micromap the accessory minerals to define compositional domains (e.g., Monazite: Y, U, Th, Ca, N).	focused beam. 0.5 mm step size.
4	Process maps: simultaneous and individual; superimpose maps onto full-section map for analysis.	
5	Select grains and domains for analysis based on compositional and microstructural significance.	
6	Recoat for quantitative analysis.	Al coat 25 nm, followed by C-coat 8 nm.
7	Quantitative analysis for full chemistry and age. Trace element methodology for Pb, U, and Th, as well as low concentration elements relevant to key reactions (see Table 3).	15 kV, 200 nA. Focused beam.

lessons learned especially with respect to trace element analysis for petrochronology. Key steps in the overall preparation and analytical procedure are summarized in Table 1.

Analytical strategy

An obvious goal in designing hardware, software, and analytical procedures for trace element analysis is to obtain the smallest possible detection limits within a practical setup/analytical timeframe. As formalized by Ziebold (1967), the propagated precision on the *k*-ratio is given by:

$$\sigma_k^2 = k^2\left[\frac{\overline{N}+\overline{N}(B)}{n\left(\overline{N}-\overline{N}(B)\right)^2}+\frac{\overline{N_s}+\overline{N_s}(B)}{n'\left(\overline{N_s}-\overline{N_s}(B)\right)^2}\right] \quad (1)$$

and similarly, the variance of the concentration is given by:

$$\sigma_C^2 = C^2\left[\frac{\overline{N}+\overline{N}(B)}{n\left(\overline{N}-\overline{N}(B)\right)^2}+\frac{\overline{N_s}+\overline{N_s}(B)}{n'\left(\overline{N_s}-\overline{N_s}(B)\right)^2}\right]\times\left[1-\frac{(a-1)C}{a}\right]^2 \quad (2)$$

where σ_k = standard deviation, N = sample peak counts, $N(B)$ = sample bkg counts, N_s = std. peak counts, $N_s(B)$ are the std. bkg counts, k = k-ratio = $(N-N(B))/(N_s-Ns(\mathrm{B}))$ for a pure element standard, n and n' = number of measured points on sample and standard, σ_c = concentration standard deviation, C = concentration, and a = correction factor that relates the k-ratio to concentration.

The relationships in Equations (1) and (2) describe the precision of the acquisition based on the Poisson statistics of X-ray emission. The equations also suggest where minor inaccuracies can strongly influence the result, particularly in the case of low-net-intensity unknowns such as trace elements. One clear implication is that the standard concentration for

trace element analysis should be as high as possible to diminish the second term in equation 1. Then, for cases of diminishing peak/background, the precision of the result depends critically on: (1) maximizing peak counts (by increasing current, voltage, counting time, spectrometer collection efficiency, increasing the number of analysis points in an acquisition), and (2) the precision of the background, which ultimately determines the signal/noise level to be overcome in order for an element to be considered detectable. Each of these will be briefly discussed below. See also Ziebold (1967), Goldstein (1967), Ancey et al. (1978), Merlet and Bodinier (1990), and Lifshin et al. (1999) for formalisms of detection limit calculations.

The precision of an analysis in EPMA is clearly dependent on optimizing the total counts collected at the characteristic wavelength (or energy) for the element of interest. The simplest approach in the acquisition of more counts is to increase beam current and/or counting time, but as with many analytical variables, there are important trade-offs. High beam current with a small beam size results in high beam power density (Jercinovic et al. 2012) and subsequent beam damage and contamination. Long count time will also exacerbate time-dependent manifestations of beam damage and contamination, and also increase the potential for instrumental drift or internal charge effects. Another option is to acquire a population of peak acquisitions within a homogeneous compositional domain. However, the potential gain diminishes as the number of points increases above approximately 6. Jercinovic et al. (2012) showed that increasing the number of analysis points from 7 to 10 for a trace element analysis of Pb resulted in an increase the sensitivity of only 2 ppm. Other approaches are also very useful, including the use of multiple spectrometer simultaneous counting of the same line, with subsequent integration of counts. In this way, quite high sensitivity is possible with reasonable counting times, for example, a detection limit of 2–3 ppm is possible for Ti in quartz by integrating 5 spectrometers in 960 s acquisitions (Donovan et al. 2011). Additionally, the types of spectrometers employed can make a substantial difference, including the use of large and very-large monochromators (and carefully adjusted counter parameters, specific to the element being analyzed), and/or smaller radius focusing geometries (sacrificing spectral resolution). Higher voltage will also increase the ionization efficiency, but with the obvious trade-off of decreased spatial resolution and the possible introduction of increased spectral complexity resulting from higher energy ionizations (see Jercinovic et al. 2008).

One realization has been evident for decades—trace element sensitivity (lowering detection limit) results from the ability to characterize background at high precision as much as it does from maximizing peak counts (Reed 1993). Simple off-peak, two-point interpolation of background will not adequately account for curvature, particularly if positions are limited in complex matrices (Jercinovic et al. 2008, 2012). Background shape, a convolution of Bremsstrahlung emission vs. wavelength and spectrometer efficiency, must be directly assessed, and must also include the recognition of even the slightest component of interference in the background measurement regions of the spectrum. The combination of background curvature and interferences can produce disastrously inaccurate trace element results (Fig. 4) if not properly accounted for (Merlet and Bodinier 1990; Jercinovic et al. 2008). Further, because of the complexity of the spectrum in minerals such as monazite, xenotime, or zircon, is it extremely difficult to recognize small background interferences even on relatively high-resolution wavelength scans (see Williams et al. 2006; Jercinovic et al. 2008). Detailed WDS scanning is essential, but not completely satisfactory unless the precision of the WDS acquisition matches the precision of the quantitative analysis. As discussed below, errors due to background interference are systematic and reproducible for the domain being analyzed. The error could be severe even if secondary standards give acceptable results, and particularly if only a single secondary standard has been evaluated.

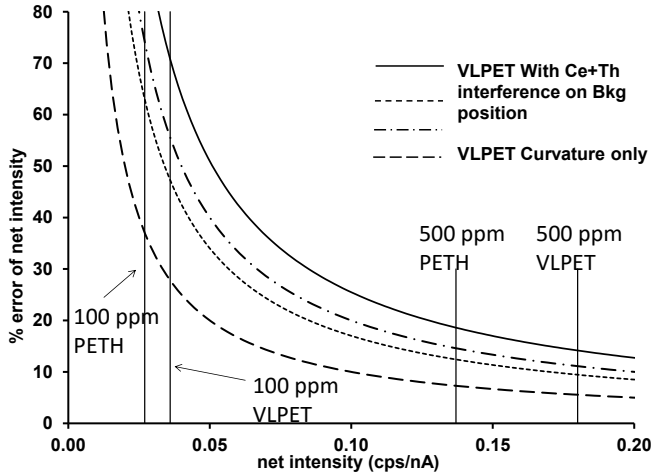

Figure 4. Growth of error (in %) on the net intensity (= Peak cps/nA – background cps/nA) as a function of net intensity for Pb Mα in monazite if a two-point linear interpolation is used. One bkg point was placed between Pb Mα and Pb Mβ, and the other at a suitable wavelength above the Pb Mα analytical line (above the interferences from first order Th $M\zeta_2$, second order La Lα, and first order S Kα lines). There are two components to the error, one arises from the curvature of the background itself (dashed curves show this component only), and the other from the subtle interference that exists between the Pb Mα and Pb Mβ wavelengths. Two different monochromators are used for this estimation: PETH is the JEOL high intensity spectrometer, and VLPET is the Cameca very large PET monochromator + extended width detector. Note that at about 1500 ppm Pb, the error is a few percent, but below 500 ppm, the error on the estimate of the net intensity grows rapidly, approaching 100% at the 10 ppm level. Modified from Jercinovic et al. (2008) [Used by permission of Elsevier from Jercinovic et al. (2008) Chemical Geology, v, 254, Fig. 18, p. 213].

One approach to background characterization involves collecting a high-resolution wavelength scan of a broad region around the peak of interest and then selecting regions that are approximately background and regressing the background value at the peak position (see Williams et al. 2006). It is important to collect a very high-resolution scan and to avoid any fast-scan mode so that per-step count times are compatible with peak counts. This method has been successful when used for all reference materials and unknowns. However, there is a certain degree of subjectivity in choosing regions to be included in the regression analysis. An alternative method, called "multipoint background acquisition" (Allaz et al. 2011), involves acquisition of background intensities at multiple wavelength positions above and below the peak position. These points are exponentially regressed and evaluated for goodness of fit. When the regression meets certain criteria, the background value at the peak position is calculated. This method has the advantage of being objective and reproducible, and the regression statistics and background intensity can be evaluated and modified retroactively if necessary.

Analytical protocol

The protocol for quantitative trace element analysis is dynamic, depending on the questions being asked (see Pyle et al. 2005; Williams et al. 2006). Count times, background acquisition strategy, coating materials, etc. must be varied as the focus on key elements shifts to address particular reactions. Beam damage at high beam power density is problematic (Jercinovic et al. 2012), therefore the tradeoffs of beam diameter (plus scattering dimensions), beam current, and coating thickness/material all must be weighed. Table 2 lists the steps involved in the full quantitative EPMA characterization of phosphates such as monazite or xenotime. Additional comments and suggestions are included in Appendix 2 (deposited with MSA).

Table 2. Analytical Protocol for EPMA Trace Element Analysis.

	Procedure	Setup
1	Coating. Samples and standards should be coated simultaneously for the best possible accuracy.	Plasma clean, then apply 20 nm Al, followed by 8 nm C.
2	Calibration. U, Th, Pb and, other major, minor, and interference calibrations as needed. After initial setup, routine recalibration is less routinely necessary as long a high quality secondary standards are available.	15 kV, 80 nA, 5 μm beam diameter.
3	Define the setup, including the use of multipoint background modeling, interference corrections, time-dependent intensity corrections, multiple spectrometer integration, and blank corrections as necessary. All elements should be acquired at each point, with count times adjusted to maximize precision for key elements.	
4	Analysis of secondary standards. This may include blanks to the protocol.	15 kV, 200 nA, focused beam.
5	Analyze unknown domain. A single homogeneous domain is analyzed at a time. Measure background (multipoint or WDS scanning). Accumulate peak measurements (typically 5–6 points) around the background location. Calculate weighted mean age, uncertainty, and MSWD.	15 kV, 200 nA, focused beam. Single background acquisition per domain.
6	Reanalyze consistency standard during and after session.	

The analytical philosophy for high-precision EPMA trace element analysis involves first, using compositional mapping to define compositionally homogeneous domains and second, independently constraining peak and background counts (count rates) at the highest possible precision. Because compositionally homogeneous domains are determined in advance by mapping key elements, it is possible to decouple peak and background measurement. For example, it has been noted that Th/LREE tends to control the relative background intensity in monazite domains, so a Th map is crucial in defining domains in monazite for background acquisition (Williams et al. 2007). Peak and background measurement strategy and protocol are developed independently for maximum precision considering sample stability. Optimally, background is measured using a multipoint regression scheme during a similar time window as peak measurements. Multiple peak measurements are made adjacent to the background position until uncertainty on the age calculations stabilizes at a minimum value (typically 5–7 peak measurements). The single background measurement is used with all peak measurements in order to calculate a single "date" for the domain. The MSWD (Mean Squared Weighted Deviation, Wendt and Carl 1991) value for the weighted mean of the multiple peak measurements provides a test of the compositional homogeneity; values significantly greater than unity generally indicate compositional heterogeneity within the analytical domain.

Error assessment

Propagated counting statistics in EPMA account for only a portion of the total uncertainty on a trace element analysis, or calculated physical parameter based on trace concentrations (i.e., temperature, pressure, or age, etc.). Systematic errors, arising particularly from instrumental factors or nonrandom analytical factors are particularly serious as they may not be detected by comparisons with secondary standards. Pyle et al. (2005) highlighted many of the factors contributing to the overall error, and in particular, suggested ways to minimize systematic errors. Williams et al. (2006) suggested that one might distinguish three components of error: (1) short-term random error—primarily counting statistics; (2) short-term systematic error—primarily from background methodology (regression models, etc.), but also coating variation and conductivity issues; (3) long-term systematic error—quality of standards and calibrations, interference correction algorithms, matrix corrections, current measurement, dead-time corrections, etc.

The first component includes primarily the propagated count statistical error. This error is readily calculated and is typically apparent from scatter in results. The third component produces errors that are fully reproducible when comparing results from the same chronometer measured on the same instrument. However, these errors may be reflected in systematic differences between the results of different dating techniques or instrument types. The second error component, as noted above, is much more problematical. It includes errors resulting from compositional effects such as peak or background interferences. They may seriously compromise results from one compositional domain but not from another, and unknowns may give erroneous results when secondary standards are accurately dated. As shown by Jercinovic et al. (2008), errors of this type could be on the order of tens of millions of years or several percent of the calculated age. Currently, relatively small, but significant, background interferences cannot be predicted from knowledge of the electromagnetic spectrum or sample composition. Thus, background estimation based on wavelength scanning or multipoint regression of all unknowns is essential for recognizing and accommodating this type of error. Careful background measurement by regression is commonly also necessary in measurements for overlap corrections on standards.

Results of EPMA geochronology have been published or presented in many venues. As with all types of geochronology, estimates of the precision and accuracy of the dates must be evaluated in light of the analytical protocol and specific components incorporated in the error estimation. In particular, systematic errors associated with background estimation (type-2 above) can be very large and are generally not included in published results. Background estimations based on any two-point interpolation have the potential for large systematic interference-related error that must be incorporated into estimates of accuracy or even comparison of age determinations. In addition, small uncertainties calculated simply by taking the mean of large numbers of measurements must be viewed with caution as this tends to yield a misleading average with inappropriate uncertainty, especially when the total range of dates is much larger than twice the calculated error estimate for a homogeneous dataset.

Because of the strong dependency on phase composition and analytical methodology, it is difficult to provide generalizations about the precision of EPMA geochronology. Uncertainties increase dramatically in U- or Th-poor chronometers and also increase in young samples because of low Pb abundance. Because trace element analysis by EPMA is essentially a measurement of minor signals above background, as peak heights diminish, minor inaccuracies in background can produce large errors in net intensity and calculated concentrations and ages. Spear et al. (2009) suggested that 2% uncertainties might be a best estimate for EPMA ages using standard hardware (and this estimate does not include background-related systematic error). Using optimized hardware, such as the SX-Ultrachron microprobe, and incorporating background regression procedures (i.e., Allaz et al. 2011), errors approaching 1% (and for older samples errors less than 1%) are possible and have been demonstrated using multiple standards analyzed by multiple techniques in multiple facilities.

The examples below show the preferred manner of presenting EPMA monazite data (see Fig. 7). Each probability density function (PDF) represents results from one compositional domain, that is, one background analysis and 5–7 peak analyses. The width of the PDF plot (the calculated 2-sigma error on the population of measurements) reflects the propagated error from peak and background analysis. The magnitude of uncertainty reflects the abundance of U, Th and Pb in the monazite domain, but large deviations from expected PDF uncertainty commonly indicate compositional heterogeneity within the domain. Weighted means can be calculated from individual dates, aggregating results from a particular generation of monazite.

APPLICATIONS AND EXAMPLES OF EPMA PETROCHRONOLOGY

Textural and compositional correlation between accessory and major phases

Compositional mapping by electron microprobe, at multiple scales, is an essential part of petrochronologic analysis regardless of the instrument or technique ultimately used for dating. As noted above, the mapping can provide the critical linkage between silicate assemblages and chronometers. For example, the linkage between Y in monazite and Y in garnet is exceedingly powerful and has been extensively used in petrochronology, especially EPMA-based studies (Pyle and Spear 2003; Foster et al. 2004; Mahan et al. 2006; Williams et al. 2007). This is partly because Y is abundant enough in monazite and garnet to be readily measured by electron probe. Also, in medium and high-grade metamorphic rocks (those without xenotime), monazite and garnet are the major hosts for Y, and thus, changes in the Y content of monazite commonly reflect modal changes in garnet, and because garnet is one of the key petrologic index minerals, constraining the timing of garnet growth and break-down events commonly provides some of the most critical timing constraints on the tectonic history.

Monazite–garnet–yttrium connection—Example 1: Legs Lake shear zone, Saskatchewan

One example of integrated compositional mapping and petrologic analysis, and the power of the Y–monazite–garnet connection, comes from Mahan et al. (2006) but has been expanded for use here. Mahan et al. (2006) investigated the timing and significance of the Legs lake shear zone, Athabasca Granulite terrane, Saskatchewan. The shear zone separates granulite facies (~1.1 GPa) rocks from amphibolite facies (~0.5 GPa) rocks. Kinematic analysis indicates oblique thrust-sense shearing of the high-grade rocks over lower-grade rocks. The granulite facies rocks contain evidence for two high-*P*–*T* tectonic events, one at ca. 2.6–2.55 Ga and one at ca 1.9 Ga. Thrusting/shearing occurred at ca. 1.85 Ga, and is interpreted to have been associated with exhumation of the granulite facies rocks. Mahan et al. (2006) calculated isochemical phase diagrams for rocks outside of and within the shear zone, and interpreted the *P*–*T* history and reaction history of the rocks during their evolution from dry deep-crustal conditions to hydrous mid-crustal conditions (Fig. 5).

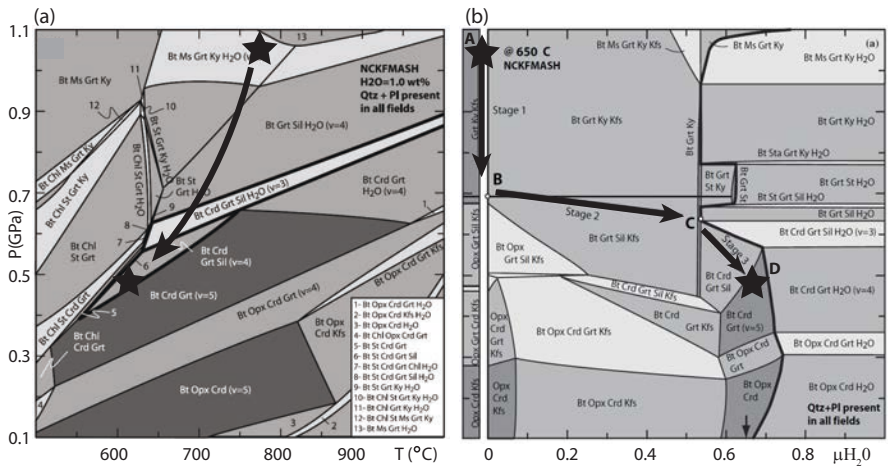

Figure 5. a) *P*–*T* isochemical phase diagram (pseudosection) for sample S32D including 1% H_2O. Black arrow shows inferred path during Legs Lake shear zone thrusting and exhumation based on peak and retrograde assemblages and reaction relationships (Mahan et al. 2006). b) *P*–M_{H_2O} pseudosection sample S32D. Black arrow shows path of decompression and hydration during Legs Lake shear zone thrusting. Thick black line marks H_2O saturation. Monazite population-5 is interpreted to reflect reaction B→C (Grt + Kfs + Pl1 + H_2O = Bt + Sil + Pl2 + Mz5 + Ap) [Used by permission of John Wiley and Sons from Mahan et al. (2006), Journal of Metamorphic Geology, v24, Figs. 6, 7, p.203,205].

Sample S32D was collected from within the Legs Lake shear zone. It preserves a particularly complete record of the metamorphic history including hydration associated with retrograde metamorphism. Figure 1 is a full-thin-section Mg Ka compositional map of sample S32D. The map shows several garnet porphyroblasts that have been fractured and partially replaced by cordierite (inside) and by biotite (outside). Stars mark the location of monazite grains, identified by full-thin section compositional mapping. Figure 3a shows the full-section map with high-resolution Y La maps of monazite grains superimposed. The maps were processed simultaneously so that intensities are comparable from grain to grain. Five monazite populations can be distinguished based on monazite composition (Fig. 6). Note that populations are here termed Mz1 through Mz5; Mahan et al. 2006 used the abbreviation pop-1 through pop-5. Monazite inclusions in garnet have been described by Mahan et al. (2006) and by Williams and Jercinovic (2012). Inclusions within innermost garnet cores are dominated by Mz1 and Mz2. Mz1 has high Y (up to several weight percent) and high Th content. Mz2 is characterized by distinctly lower Y content, reduced by at least 70%. Monazite inclusions in the outermost portions of garnet porphyroblasts are dominated by low-Y, low-Th Mz3 (Y contents of several hundred PPM or less). The very high Y content of Mz1 (comparable to monazite present in garnet absent rocks) suggests that this population probably grew before significant garnet growth. Because of the strong partitioning of Y into garnet, growth of even small amounts of garnet are associated with significant decreases of Y in monazite. The stepwise drop in Y from Mz1 to Mz2 to Mz3 (Fig. 6) is interpreted to represent two period(s) of garnet growth in the rock. This and the spatial separation of Mz2 and Mz3 within garnet suggests that these two populations may represent two distinct monazite producing reactions associated with two different garnet growth reactions. Mz3 contains the lowest Y content seen in the rock and is interpreted to represent the time of maximum garnet mode (i.e., volume percent). Th has been seen to increase from Mz2 to Mz3 in some monazite grains and to decrease in others. This may indicate the presence of limited amounts of partial melt where local access to melt yielded higher Th and isolation from melt yielded lower Th.

Most matrix monazite grains are relatively unzoned. Although rare cores of earlier monazite generations (Mz1 or Mz2) are locally present, most matrix grains are dominated by low-Y Mz4. Locally, monazite grains display high-Y rims (Mz5). These rims are generally restricted to monazite grains that are within several hundred μm of a garnet porphyroblast,

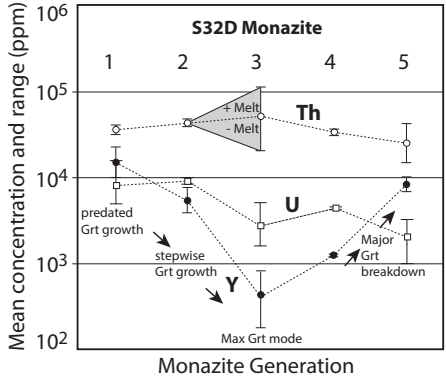

Figure 6. Plot showing variation in Y, Th and U among five monazite populations (Mz1–Mz5) in retrograde felsic granulite S32D from the Legs Lake shear zone, Athabasca area, Canada. [Used by permission of John Wiley and Sons from Mahan et al. (2006) Journal of Metamorphic Geology, v. 24, Fig. 8, p 208].

probably attesting to the limited mobility of Y in the matrix. In addition, monazite grains that are included in dynamically recrystallized plagioclase do not have the high-Y rims. This suggests that dynamic recrystallization of matrix plagioclase occurred after growth of Mz4 but before significant garnet break-down. That is, Mz4 monazite was trapped within recrystallizing plagioclase, and was shielded from later Mz5 overgrowths by the enclosing plagioclase.

Two monazite grains, of the 50 grains that were mapped, have all five populations (m14 and m48—Fig. 3). No other grain has more than three of the populations. We refer to these grains as "Rosetta-stone" grains (Dahl et al. 2005) because they are particularly important for petrochronology, i.e., linking chronology to tectonic events. Interestingly, the two grains are not among the largest monazite grains in the section, nor do they occupy the same microstructural setting. Monazite 14 occurs within the garnet rim and monazite 48 is in the matrix. Because of their small size, neither grain would probably have been recovered in a traditional mineral separation. Based on experience mapping a large number of samples from many localities, it is common to have a monazite population dominated by relatively simple one- or two-generation grains and then to have a small number of Rosetta-grains that capture important details of the history. This underscores the need to map a relatively large number of chronometer grains in a structurally and petrologically important sample.

Table 3 summarizes a set of observations that can be made from monazite compositional relationships in sample S32D. Some interpretations are rather speculative but they establish a set of hypotheses that can be tested and refined by quantitative monazite analysis and by analysis of other rocks. The next step is to document the composition and compositional variation within each monazite population and in the process, confirm that the map-defined populations are indeed homogeneous compositional populations. Then, the final step is to develop an analytical strategy to determine the age or age range for each population. This can be thought of as sampling each population, using the most appropriate geochronologic technique, in order to constrain the age.

Mahan et al. (2006) presented dates for monazite from the five populations using earlier EPMA techniques, and some new dates have been determined using techniques summarized above. Mz1, Mz2, and Mz3 are Archean (2.6–2.55 Ga) and confirm the Archean age of most garnet in the sample. Mz4 is Proterozoic (ca. 1.9 Ga), and corresponds to the second metamorphic event in the area. The presence of Mz4 inclusions in some garnet rims suggests that there may have been some Proterozoic garnet growth. Further, the very low Y content of both Mz3 and Mz4 suggests that there may not have been significant decompression (i.e., exhumation) between Mz3 and Mz4, i.e., between the Archean and the Proterozoic events. Garnet consumption associated with decompression is typically associated with growth of new Y-richer monazite. This is one piece of evidence supporting prolonged residence of the terrane in the deep crust, possibly from ca. 2.55 Ga to 1.9 Ga. Finally, high-Y Mz5 monazite constrains thrust-sense shearing and exhumation associated with the Legs Lake shear zone to have occurred between 1.9 and 1.85 Ga. The significantly increased Y in Mz5 is interpreted to reflect garnet breakdown during exhumation and decompression.

Sample S32D is an example of a "Rosetta-Stone" sample that preserves a particularly long and complete record of the tectonic history. Typical of many studies, once such a sample is discovered and characterized, other samples can fill in missing details of the *P–T–t–D* history. For example, the Legs Lake shear zone is locally cut by one other shear zone, the Grease River shear zone. Within this zone, the Legs Lake assemblages once again have been reequilibrated. Biotite plus cordierite pseudomorphs after garnet such as those in sample S32D (Fig. 1) have been flattened and deformed into the new shear-related foliation, and replacement of cordierite by chlorite and epidote documents greenschist facies conditions. One new population of monazite has developed in the late-stage structures, postdating Mz5 and constraining the age of this latest shearing event, and of greenschist facies metamorphism, to ca. 1.80 Ga (Mahan et al. 2006; Dumond et al. 2013).

Table 3. Interpretive Petrochronologic History of Sample S32D.

1. Garnet growth occurred in at least two phases, probably from two garnet-producing reactions. Monazite Mz1 predates significant garnet growth. Mz2 postdates the first garnet growth phase and Mz3 postdates the second growth phase.
2. Mz1 and Mz2 are abundant and closely spaced in all garnet cores, but few Mz1 or Mz2 remnants are present outside of the inner cores of garnet. Thus, early monazite was consumed or recrystallized before growth of Mz3. This may represent a stage of melting as suggested by the synchronous growth of new garnet and high-Th nature of monazite Mz3.
3. The efficient removal of early monazite may also indicate a deformation phase between Mz2 and Mz3.
4. Little new garnet growth occurred after Mz3. Mz3 records the lowest Y (and Gd) contents of all monazite populations.
5. The similar Y-content of Mz3 and Mz4 suggests that little garnet consumption occurred between these two monazite populations.
6. Matrix monazite is dominated by Mz4, with few cores or remnants of earlier populations. This suggests a second period of efficient monazite consumption after Mz3 and after garnet growth.
7. Dynamically recrystallized plagioclase wraps around garnet and contains only Mz4 monazite. Deformation and recrystallization occurred during or after Mz4 and before Mz5. Plagioclase is unzoned and thus the composition equilibrated with Mz4–Mz5 phases.
8. Mz5 was associated with garnet consumption as indicated by the major increase in Y. Mz5 rims are not aligned with dominant fabric; many occur on perpendicular sectors. This the dominant matrix deformation had terminated before Mz5. This is consistent with the persistence of abundant early monazite.
9. Cordierite in garnet fractures contains inclusions of xenotime. Thus, at least the later stages of cordierite replacement of garnet occurred below the monazite ⇒ xenotime reaction.

Monazite–garnet–Y connection. Example-2: dating deformation

Figure 7 is one example of EMPA reaction dating following the protocol described above and modified from Williams and Jercinovic (2012). The basic question concerned the timing of folding and of garnet growth in a metamorphosed sediment from the Northwest Territories, Canada. Inclusion fabrics suggest that garnet grew during folding of an earlier fabric (S1) that was sub-parallel to compositional layering. Based on Y and Th content, three generations of monazite were distinguished, one pre-garnet, one syn-garnet, and one post garnet. Once the timing hypothesis was formulated, each generation was analyzed several times and dates calculated. Figure 7b show results for pre and post-garnet domains and Figure 7c shows syn-garnet results superimposed. Taken together the results show that garnet growth and folding occurred at ca. 1900 Ma. and retrogression began soon afterward. As noted above, Figure 7 also shows the preferred manner of presenting EPMA monazite data.

Other compositional/textural linkages with silicate assemblages

Recently, a broader suite of trace elements and element ratios have been used to link monazite with silicate assemblages in EPMA-based and also in LA-ICP-MS-based studies. Th content in monazite may be particularly useful as a monitor of melting reactions. Th is partitioned into the melt phase relative to the residual phases especially for haplogranite melts (Keppler and Wyllie 1990; Stepanov et al. 2012), but Th is partitioned into monazite relative to haplogranite melt, i.e., the monazite/melt partitioning coefficient is greater than unity (Rapp et al. 1987; Xing et al. 2013). In addition, the solubility of monazite in granitic melt has been interpreted to decrease with increasing pressure (Dumond et al. 2015). This suggests

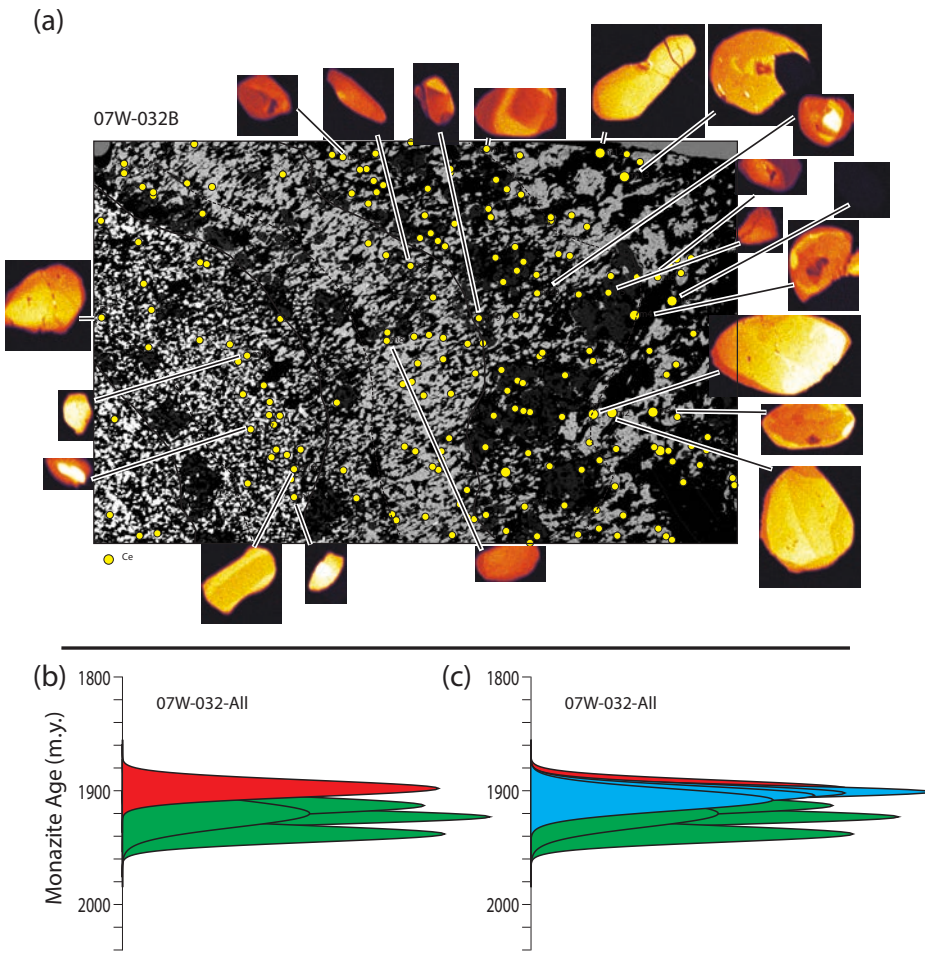

Figure 7. Monazite geochronology from west of Snowbird Lake, Northwest Territories, Canada. (a) Ca Kα WDS full-thin-section compositional map showing folded early compositional layering and axial plane S2 cleavage. High-resolution Y Lα compositional maps superimposed. Note, some grains are parallel to S1/S0 (also defined by inclusions in garnet), and some grains are parallel to S2 (upper left to lower right). Zoning in monazite is much more pronounced in Grt-rich layers. (b) Microprobe monazite geochronology. Each probability distribution plot represents one monazite date, including one background and 5–8 peak analyses (see text for discussion). Green curves are grains that are early with respect to S2 cleavage and garnet growth. Red curve is late with respect to S2 cleavage. (c) Same plot as (b) with addition of dates for syn-S2 and syn-garnet monazite. S2 cleavage and peak metamorphism (garnet growth) are constrained to be ca. 1900±8 Ma. Early stage of exhumation and garnet consumption are constrained to 1893±12 Ma. Modified from Williams and Jercinovic (2012). [Used by permission of John Wiley and Sons, Williams and Jercinovic (2012) Journal of Metamorphic Geology, v30, Fig 5, p. 749].

that at higher pressures, monazite may provide key constraints on the timing and character of melt reactions. For example, Dumond et al. (2015) used phase equilibria to characterize melting reactions, adjust bulk compositions for melt loss, and interpret *P–T–t–D* histories for high-*T* granulite facies migmatites from the Athabasca Granulite Terrane (Fig. 8). They used multi-scale compositional mapping to integrate monazite into the reaction and melting history. The rocks contain multiple generations of monazite. The earliest generation is interpreted to

represent detrital/inherited monazite. High-Th, low-Y monazite was interpreted to have been produced during biotite dehydration melting. Sharp drops in Th in later monazite generations were interpreted to reflect melt loss from the system, i.e., significant drops in bulk-rock Th content (Fig. 8). Thus, Th in monazite may not only serve as a monitor of melting but also of melt-extraction events in high-grade metamorphic rocks (Dumond et al. 2015).

More speculatively, Dumond et al. (2010, 2015) suggested that elevated Eu (and positive Eu anomalies) in monazite may be related to plagioclase break-down and to some degree, to sequestering of heavy REEs into garnet. In addition, light REE (especially Ce and La) enrichment has been suggested to be related to feldspar loss or recrystallization (Dumond et al. 2015; also see Bea 1996; Villaseca et al. 2003). These observations suggest a linkage between monazite and feldspar that may further allow monazite generations to be integrated into silicate reactions.

Because of the limited mobility of Rare Earth elements, especially in relatively dry rocks, it may be particularly useful to distinguish and compare different compositional layers or domains in rocks. For example, in the eastern Adirondack Mountains, monazite in garnet-rich gneiss has high-Y rims while in strongly recrystallized and lineated K-feldspar-rich layers monazite rims are subtly enriched in U. The increased U is interpreted to have been hosted by feldspar before recrystallization. The garnet rich and K-feldspar rich layers share a common fabric,

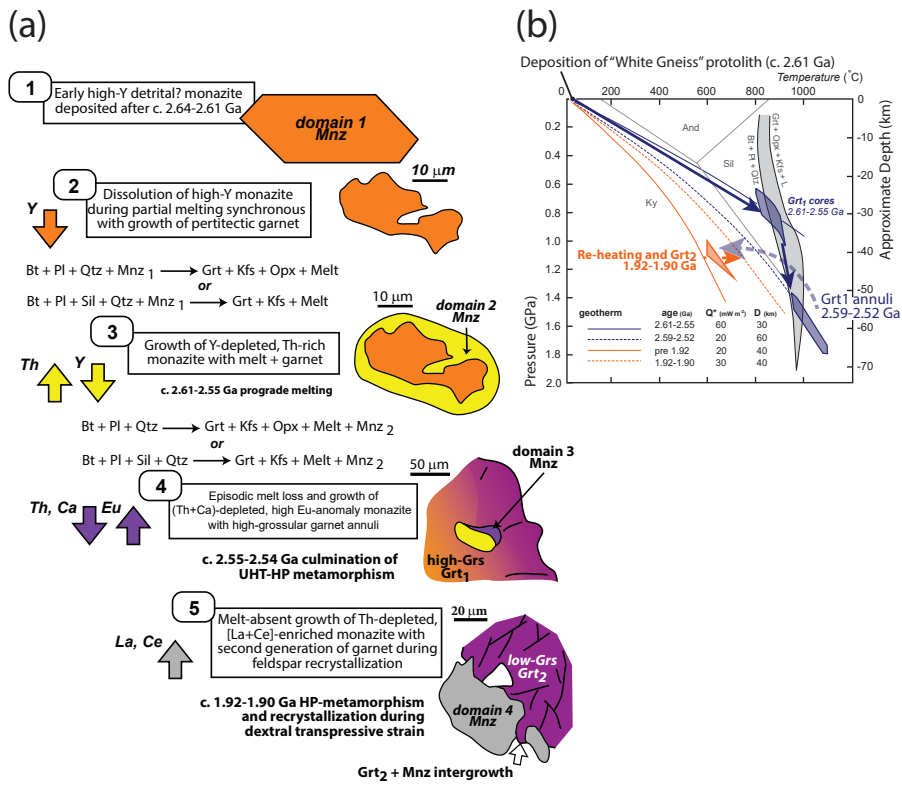

Figure 8. (a) Interpreted monazite reaction history and geochemical linkages with garnet generations and melting in high-*T* granulite facies migmatites from the Athabasca Granulite Terrane, Saskatchewan. (b) Interpreted *P–T* history based on petrologic modeling and monazite geochronology. See text for discussion. Modified from Dumond et al. (2015). [Used by permission of John Wiley and Sons from Dumond et al. (2015) Figures 15, 16, v.33, p 755–756].

mineral lineation, and kinematic shear sense, and both types of monazite rims have similar ages (Wong et al. 2012). Taken together, the two layer types suggest that garnet consumption (i.e., decompression), K-feldspar recrystallization, and extensional shearing were all synchronous. This allows the earliest phases of extensional shearing to be constrained and tied to early garnet resorption and exhumation in the eastern Adirondack Mountains (Wong et al. 2012).

In some samples, the limited mobility of trace elements is particularly apparent. An Al-rich gneissic sample from the Adirondack Mountains is distinctly layered with garnet-rich and garnet-poor layers. Monazite composition and dates are dramatically different from layer to layer. At least three distinct layer types can be recognized (Fig. 9). Layer-1 preserves only relatively young monazite that largely reflects the early stages of exhumation. This layer may have experienced more intense, late-stage strain, removing older monazite and promoting growth or recrystallization of new monazite. Layer-2 preserves older monazite (1180–1150 Ma). These are present as inclusions in garnet and also as matrix grains. It may be that these garnet-rich layers were stronger and thus less deformed during the late-stage deformation events. Layer-3 preserves a heterogeneous assemblage of monazite with dates that are more difficult to interpret. Some of these grains bear the unmistakable signature of dissolution-reprecipitation (see below) suggesting that this layer was affected by fluids of the right composition to interact with monazite (Harlov and Hetherington 2010; Williams et al. 2011). Taken together, monazite in this sample provides a very complete record of the petro-tectonic history from early high-grade metamorphism to late extensional collapse, but without careful multiscale mapping and in-situ analysis, accurate analyses would be impossible and the results would be very difficult to interpret.

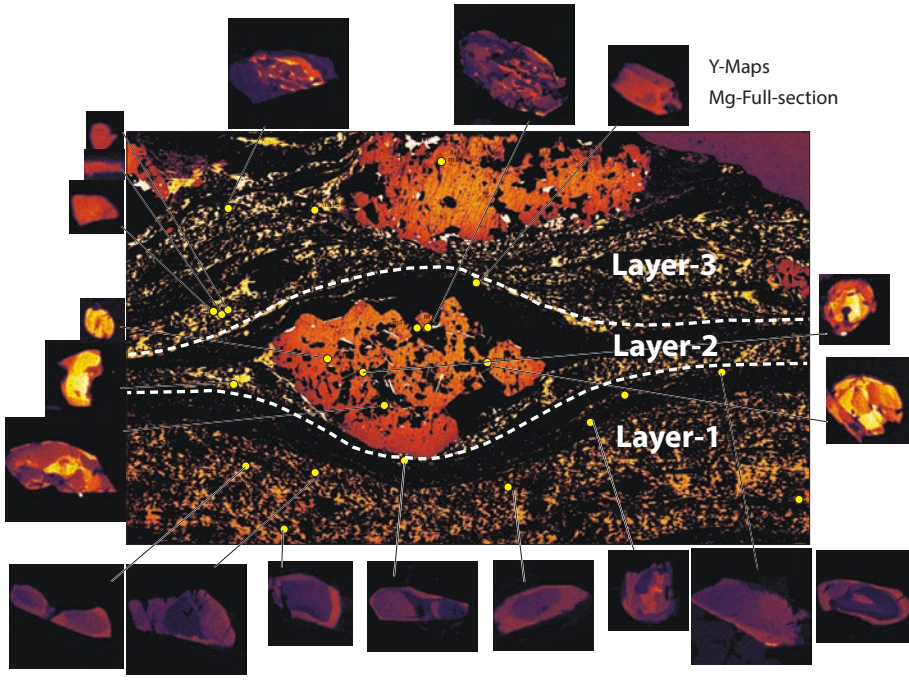

Figure 9. Full-section Mg Kα compositional map of Sample 85-1 (Adirondack Mountains) with Y Lα maps of monazite grains. Three different layer types have distinct monazite compositions and ages. Layer-1 grains contain exclusively 1050 Ma cores and 1030 Ma rims. Layer-2 grains have 1180 Ma core and 1150 Ma rims. Layer-3 grains have 1030 Ma domains and 980 Ma domains and complex textures characteristic of fluid-related recrystallization.

EPMA PETROCHRONOLOGY COMBINED WITH ISOTOPIC ANALYSIS

The electron microprobe also plays a major role in petrochronologic analysis in studies where the electron probe cannot be used for dating. Monazite and xenotime in relatively young metamorphic or igneous rocks (younger than approximately 100 m.y.) is generally not amenable to EPMA dating because of low Pb abundance. However, electron microprobe mapping and analysis of the chronometer phases and evaluation of the local reaction context are critical to drawing conclusions about the *P–T–t–D* history. Many studies in relatively young rocks have involved electron microprobe mapping and analysis followed by isotopic analysis by ion microprobe (i.e., see references in Vance et al. 2003; Kohn et al. 2005) or LA-ICP-MS (i.e., Larson et al. 2011; Regis et al. 2016). One of the disadvantages of this type of analysis is that many early core domains and late rim domains in chronometer phases are very small or narrow even for a focused laser or ion microprobe. Compositional mapping of a larger number of chronometer phases and identification of generations allow relatively larger domains to be dated and then correlated with smaller domains in distinctive structural or petrological setting.

Titanite is known to contain significant amounts of common Pb and thus cannot be readily dated using a total-Pb method such as electron microprobe dating. However, titanite compositions can vary widely and can be integrated into silicate reactions. Titanite is certainly amenable to the type of multi-scale compositional mapping and textural analysis as presented above for monazite. For example, Wintsch et al. (2005) used compositional mapping to identify several generations of titanite in granodioritic orthogneiss in Connecticut. The authors interpreted a reaction involving replacement of metastable magmatic K-feldspar, hastingsite, magnetite, and titanite by new metamorphic biotite, epidote, quartz and metamorphic titanite. Specifically, titanite was interpreted to have been produced by a reaction such as clinozoisite = plagioclase + Al-dominant titanite (Wintsch et al. 2005), and comparisons of REE composition of titanite and epidote were used to distinguish titanite generations. EPMA and SEM images were used to select Al-richer and Al-poorer titanite dating targets. Then, SHRIMP U–Pb dating was used to constrain ages. Although this is an example of petrochronology involving the electron microprobe, it is suspected that even more insight into the nature and relative timing of titanite producing reactions would result from integrated multiscale image analysis such as that described above.

One additional petrochronology application that involves an important component of EPMA analysis and also has great future potential is ^{40}Ar–^{39}Ar dating of mica, hornblende, and other K-bearing phases. The electron microprobe has been used to identify and distinguish compositional populations of micas or amphiboles and to generate phase diagrams incorporating the stability of different generations of these phases. Then, ages have been obtained by one of several possible methods: (1) in-situ laser techniques, (2) carefully micro-sampling distinct structural/petrologic domains, or (3) by interpreting distinct ages from step-heating results (e.g., Villa et al. 2000; Müller et al. 2002; White and Hodges 2003; Condon et al. 2006; Flowers et al. 2006b; Wells et al. 2008; Growdon et al. 2013; Schneider et al. 2013; Lanari et al. 2014; Chafe et al. 2014; Villa et al. 2014). One important strength of this approach is the possibility to exploit the ^{37}Ar–^{38}Ar–^{39}Ar correlation diagrams to fingerprint phases, and so to integrate deformation stages, as defined by mica fabrics and heterochemical generations, with *P–T* histories (Villa and Williams 2012).

Because K-feldspar, biotite, and especially white mica and amphibole can preserve microstructural relicts and the associated isotope inheritance even under medium and high-*T* conditions, all while new heterochemical mineral generations are growing, K–Ar chronometers are not substantially different from U–Pb chronometers such as monazite (Villa and Williams 2012), as both are "Class II" mineral chronometers (Villa 2016). ^{40}Ar–^{39}Ar chronology, in combination with detailed petrological characterization and dating of other geochronometer

systems, has been particularly useful for constraining the retrogression history all the way from upper amphibolite facies to sub-greenschist facies. As new micas and feldspars tend to grow during retrograde events that take place relatively late, they have been used to constrain the exhumation stages of tectonic histories (i.e., White and Hodges 2003; Flowers et al. 2006b).

LOW-GRADE METAMORPHISM AND FLUID–ROCK INTERACTION

Many of the examples discussed above involve medium and high-grade metamorphism where reactions involving silicates and chronometer phases have been interpreted. Another rich avenue for petrochronologic study, and EPMA petrochronology, is in low-grade metamorphic rocks and hydrothermal processes. A number of reactions have been interpreted during diagenesis or low-grade metamorphism including: alteration of detrital monazite and growth of allanite, alteration of detrital monazite and growth of new monazite, growth of xenotime on detrital zircon, and growth of new generations of monazite, xenotime, or zircon during fluid infiltration events (Rasmussen 1996; Vallini et al. 2002; Rasmussen and Muhling 2007, 2009; Janots et al. 2007; Rasmussen et al. 2007; Allaz et al. 2013). In each case, detailed textural and compositional analysis of the chronometer phases have shed light on the nature and timing of digenetic and low-grade metamorphic reactions. Commonly, the authigenetic, digenetic, or low-grade metamorphic chronometer phases are very fine grained (less than 10 mm). The electron microprobe or SEM can be essential for simply finding and identifying the minerals and for quantifying compositions and ages. One of the most common applications of petrochronology in low-grade rocks is in dating and characterizing economic mineral and ore deposits (i.e., Rasmussen et al. 2006; Muhling et al. 2012; Zi et al. 2015).

Diffusional resetting of monazite, zircon, or xenotime ages is considered unlikely under most geological conditions because of extremely slow diffusion (Cherniak et al. 2004; Cherniak and Pyle 2008; Cherniak 2010). However, experimental work and empirical observations suggest that it is possible to reset zircon, monazite, and xenotime through dissolution-precipitation mechanisms (Seydoux-Guillaume et al. 2012; Villa and Williams 2012; Didier et al. 2013; Ruiz-Agudo et al. 2014), and that resetting may occur over a range of metamorphic grades (Harlov and Forster 2002; Harlov et al. 2007, 2011; Hetherington et al. 2008; Harlov and Hetherington 2010; Williams et al. 2011; Kelley et al. 2012). These observations have important implications for petrochronology because reset (recrystallized) chronometers may not be in equilibrium with the associated silicate assemblage and thus, may lead to incorrect timing constraints on the petrologic history (see Villa and Williams 2012). However, they also suggest a new avenue in petrochronology, that is, the accessory phases can place constraints on composition, character, and especially the timing of fluid–rock interactions (Grand'Homme et al. 2016).

The electron microprobe also has a role to play in identifying and characterizing the products of these dissolution-precipitation reactions. First, it is critical to recognize domains in zircon or monazite that have undergone dissolution-precipitation. The regions can have remarkably straight and crystallographically controlled boundaries and can be easily mistaken for overgrowth domains (see Harlov et al. 2011; Williams et al. 2011; Villa and Williams 2012). However, high-resolution compositional mapping and backscattered electron imaging can show narrow reset domains that follow inclusion trails, or cracks, and locally form delicate fingers intruding the core domains. Further, reset domains commonly have a distinctive composition, typically characterized by a more nearly end-member monazite, xenotime, or zircon composition than the host crystal (see discussion in Williams et al. 2011; also Didier et al. 2013). The electron microprobe can be used to investigate the composition of very small altered domains and for older chronometers to constrain the age of the alteration.

FUTURE TRENDS IN EPMA PETROCHRONOLOGY

Electron microprobe instrumental aspects

Electron Probe Micro-Analysis (EPMA) is a time-honored electron beam technique for the non-destructive quantitative analysis of micro-volumes in-situ. Since its inception in 1950, hardware, software, and physical theory have all advanced considerably, and continue to evolve to this day. Many advances are the result of technological improvements that have been inspired by the needs of the scientific community, and have primarily been aimed at improving sensitivity, accuracy, spatial resolution, and efficiency. For high spatial resolution trace element analysis and geochronology, a number of developments (some already in progress) can increase the sensitivity, spatial resolution, and especially, the efficiency of compositional mapping and quantitative analysis that are important for petrochronologic studies.

One recent emphasis centers around the improvement and refinement of low energy X-ray detection and quantification in order to exploit the low scattering volumes attainable at low accelerating voltage, resulting in higher analytical spatial resolution (e.g., McSwiggen et al. 2011; Armstrong et al. 2013; Hombourger and Outrequin 2013; Gopon et al. 2013; Susan et al. 2015). This development has been inspired in part by improvements in application of higher brightness sources (rare earth hexaboride and Schottky field emitters). However, the challenges are formidable particularly in trace element analysis, in which case high beam current and/or long counting time can compromise accuracy at high current density (Jercinovic et al. 2012), and more generally in evaluating soft X-ray spectra resulting from valence band transitions (Burgess et al. 2014; MacRae et al. 2016a,b). We expect significant progress over the next decade in the quantification of these difficult spectral emission regions, and regardless of difficulties in quantification, high spatial resolution mapping is extremely valuable. Quantification of WDS/EDS map data is also developing rapidly, even becoming useful in trace element applications (e.g., Donovan et al. 2016). The approach to petrochronologic studies with EPMA is mapping centric, and improvements in mapping efficiency, performance, signal integration (e.g., MacRae et al. 2016a) or processing will be advantageous, including rapid simultaneous processing (see Williams et al. 2006) of large sets of maps from multiple samples in characterizing geologic terrains.

The spectrometers currently deployed on WDS instruments cover just about any need, but there is room for improvement in terms of collection efficiency, specifically optimized monochromators, or detector gases and pressures for certain elements or element ranges and/or suppression of high order diffraction effects. These issues involve both high energy and low energy detection, for example, there are reasons to explore more efficient detection of the uranium L series using LIF [220], topaz [303], or α-quartz [20$\bar{2}$3], particularly in low Th monazite, xenotime, or zircon analysis. As discussed above, there is also renewed emphasis on low energy X-ray detection, including parallel beam optics (e.g., LEXS [EDAX, Inc.]), grating optics with CCD photon counters (Terauchi et al. 2012; MacRae et al. 2016b; Robertson and McSwiggen 2016), adaptation of silicon drift detector (SDD) technology to WDS (Moran and Wuhrer 2016), which may help both in improving collection efficiency as well as spectral resolution (e.g., Hombourger and Outrequin 2013; Robertson and McSwiggen, 2016). Obviously continued improvement in the energy resolution in energy dispersive detectors, and refinement of energy dispersive spectrometry for full integration into WDS based systems will be important particularly in improving efficiency for rapid analysis of many chronometer phases from multiple samples. So-called hyperspectral mapping datasets that combine signals for phase identification/classification offer a powerful approach to large scale mapping projects involving multiphase materials significant to petrochronology (e.g., MacRae et al. 2016c). This approach will undoubtedly gain significance in routine EPMA sample evaluation. In addition, EDS may be routinely employed in determination of actual accelerating potential in low kV systems,

particularly where sample biasing is used to lower landing voltage and matrix corrections may be compromised at such low overvoltage if beam voltage is not accurately known.

Dual or multi-beam systems, and continued development of high performance sources will likewise be important in EPMA-based petrochronologic studies. Electron-laser dual beam integration may become tenable, allowing initial mapping and elemental analysis by EPMA, followed by high sensitivity LA mass spectrometry for further trace element evaluation and isotopic analysis. Continued development of electron sources for higher brightness at higher, more stable current, along with continued improvements in lowering energy spread for lowering chromatic aberration and improved performance at low kV. Multi-beam characterization machines are already finding use in life sciences, and may find utility in extremely high resolution geologic sample characterization as well, allowing detailed compositional analysis not accessible by X-ray tomography, and a scale not practicable by tomographic atom probe (Eberle et al. 2015).

As mentioned above, the very high current density required for high sensitivity—high spatial resolution trace element analysis is problematic. Therefore, continued exploration of surface conductive coatings and anti-contamination are an important frontier. In particular, as beam landing energy is lowered, more of the interaction volume involves interaction with the conductive coating along with enhanced contamination effects (e.g., Gopon et al. 2013). Advanced materials based on nanostructures such as graphene or stanine for high electrical and thermal conductivity may be developed that provide reliable surfaces for microanalysis (Park et al. 2016). Low contamination vacuum systems have improved remarkably over the past few decades, and improvements in vacuum technology will continue to provide even cleaner environments. Likewise, improvements in mounting media may replace epoxies that release carbon under vacuum and beam exposure. Anticontamination systems are already commonplace, and continue to be evaluated and improved. Advancements such as plasma cleaners are increasingly common in SEMs for low kV characterization, and are now being considered for EPMA instruments, as could other methods for sputtering or actively removing contaminants.

EPMA instrumentation includes electron detectors, specifically separate secondary and backscattered detectors. However, electron microscopy has benefited greatly from newer detection systems to better allow interrogation of the full electron spectrum at tunable energies to enhance phase contrast. These include in-lens designs that can offer energy discrimination as well as having the advantage of being less exposed to contaminants in the sample chamber. For petrochronology, any advancement in phase imaging is potentially useful.

Software development always plays an important role in advancing analytical technologies, and EPMA continues to see many exceptional improvements affecting all areas of data acquisition and processing. Improvements in mapping software that permit very rapid acquisition of a broad array of X-ray and other signals (electron, IR, visible, UV, EBSD, etc.), automatic identification and location of accessory phases, and even automated mapping of these phases at high resolution (e.g., MacRae et al. 2016c). Such mapping could potentially also take advantage of techniques devised to limit beam exposure to the grains of interest only (polygon or other shape-limited beam or stage motion), and potentially improve analytical efficiency significantly.

Thermochemical aspects

One major goal of future petrochronology research is to establish the thermodynamic properties and phase relationships of accessory chronometer phases. That is, to quantitatively incorporate accessory phases into phase diagrams. Thermodynamic modeling with modified thermodynamic databases such as that done by Spear and coworkers (Spear and Pyle 2010; Spear 2010) or Kelsey (i.e., Kelsey et al. 2008; Kelsey and Powell 2011) are pioneering studies in this context. In addition, experimental studies constraining phase relationships and trace-element partitioning (i.e., Rubatto and Hermann 2007; Stepanov et al. 2012) are needed to provide critical thermodynamic data and stability relationships.

New dissolution-precipitation experiments, such as those carried out by Harlov and coworkers (Harlov et al. 2007, 2011) are needed in order to better illuminate the controls on accessory phase recrystallization and replacement and importantly, the composition of the reactive fluids. Subtle differences in fluid composition can have a significant effect on the degree of recrystallization (Harlov and Hetherington 2010). This certainly can complicate petrochronological studies but also will provide new avenues for constraining fluid–rock interactions (Rasmussen et al. 2007; Rasmussen and Muhling 2009; Peterman et al. 2016).

A first step toward better integrating accessory phases into petrologic phase diagrams involves constraining, even qualitatively, the reactions that produce chronometer phases. The electron microprobe can quantify the more abundant trace elements in chronometers including monazite, titanite, xenotime, and zircon. However, the trend is clearly toward incorporating the broadest suite of trace elements possible. We see a future involving a combination of high-spatial resolution EPMA characterization with LA-ICP-MS analysis of larger domains for greater compositional resolution. It is important to stress that the electron microprobe is unsurpassed as a tool for characterizing spatial/compositional relationships by X-ray mapping in situ, the absolutely critical first step in petrochronology. Trace elements in associated silicate phases will generally need to be evaluated by LA-ICP-MS or ion microprobe. The classic studies of Bea are seminal (Bea et al. 1994; Bea 1996), but many more are needed, particularly those in which pre- and post-reaction compositions of silicate phases can be characterized. In all cases, these trace element studies need to be closely integrated with in-situ characterization and compositional mapping of accessory and silicate phases. As noted above, trace element mapping of silicate phases holds great potential, and in certain minerals, can be readily made by electron microprobe. For less abundant trace elements and less stable silicates, LA-ICP-MS (i.e., Koening 2010; Ubide et al. 2015; Kylander-Clark 2017; Lanari and Engi 2017), ion microprobe, or even synchrotron X-ray mapping (i.e., Dyl et al. 2014) may be necessary.

One major challenge for integrating accessory and silicate phases involves the different scales (and degrees) of equilibrium for trace elements and for major elements and even for different trace elements (Berger et al. 2005). Compositions of accessory phases may reflect a much smaller equilibrium domain and a more restricted assemblage compared to the silicate phases. Bulk-rock analyses from hand samples or thin-section chips have generally been extensively used for forward modeling of silicate assemblages. For trace element modeling, evaluation of local compositional subdomains may be more important (for example see Chernoff and Carlson 1999). Multiscale compositional mapping, including trace-element mapping, and analysis by electron microprobe is ever more essential for evaluating equilibrium domains and for selecting chronometer domains that reflect specific reactions (i.e., Fig. 9). New dating techniques and instrumentation will undoubtedly be developed allowing smaller and smaller domains to be dated more and more precisely. Because of its spatial resolution and increasing efficiency in major and trace element capability it is also clear that the EPMA will play a central role in petrologic and petrochronologic analysis for the foreseeable future.

ACKNOWLEDGMENTS

The authors sincerely than Harold Stowell, Philippe Goncalves, Igor Villa, and an anonymous reviewer for their careful and helpful review comments. In addition, we sincerely thank Pierre Lanari for excellent review comments and editorial handling. Jeffrey Webber and Sean Regan are thanked for their contributions to this research and for reading an earlier draft of the manuscript. The research presented in this manuscript was partly supported by NSF grants NSF/EAR-1419843 and NSF/EAR-1419876 to M.L. Williams for research in norther Saskatchewan and the Adirondack Mountains respectively.

REFERENCES

Allaz J, Williams ML, Jercinovic MJ, Donovan J (2011) A new technique for electron microprobe trace element analysis: the multipoint background method. EMAS Annual Meeting, Angers (France)

Allaz J, Selleck B, Williams ML, Jercinovic MJ (2013) Dating fluid events through the microprobe dating of detrital monazite from the Potsdam Sandstone, NY, USA. Am Mineral 98:1106–1119

Ancey M, Bastenaire F, Tixier R (1978) Application des methodes statistiques en microanalyse. *In*: Microanalyse, Microscopie Eléctronique à Balayage. Maurice F, Meny L, Tixier R, (eds). Les Exlitions du Physicien, Orsay, p 323–347

Armstrong JT, McSwiggen P, Nielsen3 C (2013) A thermal field-emission electron probe microanalyzer for improved analytical spatial resolution. Microsc Anal 27:18–22

Asami M, Suzuki K, Adachi M (1996) Monazite ages by the chemical Th-U-total Pb isochron method for pelitic gneisses from the eastern Sor Rondane Mountains, East Antarctica. Proc NIPR Symp Antarct Geosci 9:49–64

Bea F (1996) Residence of REE, Y, Th and U in granites and crustal protoliths; Implications for the chemistry of crustal melts. J Petrol 37:521–552, doi:10.1093/petrology/37.3.521

Bea F, Montero P (1999) Behavior of accessory phases and redistribution of Zr, REE, Y, Th, and U during metamorphism and partial melting of metapelites in the lower crust: an example from the Kinzigite Formation of Ivrea-Verbano, NW Italy. Geochim Cosmochim Acta 63:1133–1153, doi:10.1016/S0016-7037(98)00292–0

Bea F, Pereira MD, Stroh A (1994) Mineral/leucosome trace-element partitioning in a peraluminous migmatite (a laser ablation–ICP-MS study). Chem Geol 117:291–312, doi:10.1016/0009–2541(94)90133–3

Bea F, Montero P, Garuti G, Zacharini F (1997) Pressure-Dependence of Rare Earth Element Distribution in Amphibolite- and Granulite- Grade Garnets. A LA-ICP-MS Study. Geostand Newslett 21:253–270, doi:10.1111/j.1751-908X.1997.tb00674.x

Berger A, Scherrer NC, Bussy F (2005) Equilibration and disequilibration between monazite and garnet: indication from phase-composition and quantitative texture analysis. J Metamorph Geol 23:865–880, doi:10.1111/j.1525–1314.2005.00614.x

Bowles JFW (1990) Microanalytical methods in mineralogy and geochemistry age dating of individual grains of uraninite in rocks from electron microprobe analyses. Chem Geol 83:47–53, doi:10.1016/0009–2541(90)90139-X

Budzyń B, Harlov DE, Williams ML, Jercinovic MJ (2011) Experimental determination of stability relations between monazite, fluorapatite, allanite, and REE-epidote as a function of pressure, temperature, and fluid composition. Am Mineral 96:1547–1567, doi:10.2138/am.2011.3741

Buick IS, Clark C, Rubatto D, Hermann J, Pandit M, Hand M (2010) Constraints on the Proterozoic evolution of the Aravalli–Delhi Orogenic belt (NW India) from monazite geochronology and mineral trace element geochemistry. Lithos 120:511–528, doi:10.1016/j.lithos.2010.09.011

Burgess S, Li X, Holland J, Statham P, Bhadare S, Birtwistle D, Protheroe A (2014) Development of soft X-ray microanalysis using windowless SDD technology. Microsc Microanal 20 (suppl 3):1–2

Catlos EJ (2013) Versatile Monazite: resolving geological records and solving challenges in materials science. Generalizations about monazite: Implications for geochronologic studies. Am Mineral 98:819–832, doi:10.2138/am.2013.4336

Chafe AN, Villa IM, Hanchar JM, Wirth R (2014) A re-examination of petrogenesis and $^{40}Ar/^{39}Ar$ systematics in the Chain of Ponds K-feldspar: "diffusion domain" archetype versus polyphase hygrochronology. Contrib Mineral Petrol 167:1010, doi:10.1007/s00410-014-1010-x

Cherniak DJ (2010) Cation diffusion in feldspars. Rev Mineral Geochem 72:691–733

Cherniak DJ, Pyle JM (2008) Th diffusion in monazite. Chem Geol 256:52–61

Cherniak DJ, Watson EB, Grove M, Harrison TM (2004) Pb diffusion in monazite: a combined RBS/SIMS study. Geochim Cosmochim Acta 68:829–840

Chernoff CB, Carlson WD (1999) Trace element zoning as a record of chemical disequilibrium during garnet growth. Geology 27:555–558, doi:10.1130/0091–7613(1999)027<0555:tezaar>2.3.co;2

Clarke GL, Daczko NR, Nockolds C (2001) A method for applying matrix corrections to X-ray intensity maps using the Bence–Albee algorithm and Matlab. J Metamorph Geol 19:635–644, doi:10.1046/j.0263–4929.2001.00336.x

Cocherie A, Legendre O, Peucat JJ, Kouamelan A (1998) Geochronology of polygenetic monazites constrained by in situ electron microprobe Th–U–Total Pb determination: implications for Pb behavior in monazite. Geochim Cosmochim Acta 62:2475–2497

Condon DJ, Hodges KV, Alsop GI, White A (2006) Laser ablation $^{40}Ar/^{39}Ar$ dating of metamorphic fabrics in the Caledonides of North Ireland. J Geol Soc London 163:337–345, doi:10.1144/0016-764904-066

Dahl PS, Hamilton MA, Jercinovic MJ, Terry MP, Williams ML, Frei R (2005) Comparative isotopic and chemical geochronometry of monazite, with implications for U–Th–Pb dating by electron microprobe; an example from metamorphic rocks of the eastern Wyoming Craton (USA). Am Mineral 90:619–638

De Andrade V, Vidal O, Lewin E, O'Brien P, Agard P (2006) Quantification of electron microprobe compositional maps of rock thin sections: an optimized method and examples. J Metamorph Geol 24:655–668, doi:10.1111/j.1525–1314.2006.00660.x

Didier A, Bosse V, Boulvais P, Bouloton J, Paquette J-L, Montel J-M, Devidal J-L (2013) Disturbance versus preservation of U–Th–Pb ages in monazite during fluid–rock interaction: textural, chemical and isotopic in situ study in microgranites (Velay Dome, France). Contrib Mineral Petrol 165:1051–1072, doi:10.1007/s00410-012-0847-0

Donovan JJ, Lowers HA, Rusk BG (2011) Improved electron probe microanalysis of trace elements in quartz. Am Mineral 96:274–282, doi:10.2138/am.2011.3631

Donovan JJ, Singer JW, Armstrong JT (2016) EPMA method for fast trace element analysis in simple matrices. Am Mineral 101:1839–1853

Dumond, G. PG, Williams ML, Jercinovic MJ (2010) Subhorizontal fabric in exhumed continental lower crust and implications for lower crustal flow: Athabasca granulite terrane, western Canadian Shield. Tectonics 29 TC2006, doi:10.1029/2009TC002514

Dumond G, Mahan KH, Williams ML, Jercinovic MJ (2013) Transpressive uplift and exhumation of continental lower crust revealed by synkinematic monazite reactions. Lithosphere 5:507–512, doi:10.1130/l292.1

Dumond G, Goncalves P, Williams ML, Jercinovic MJ (2015) Monazite as a monitor of melting, garnet growth and feldspar recrystallization in continental lower crust. J Metamorph Geol 33:735–762, doi:10.1111/jmg.12150

Dyl KA, Cleverley JS, Bland PA, Ryan CG, Fisher LA, Hough RM (2014) Quantified, whole section trace element mapping of carbonaceous chondrites by synchrotron X-ray fluorescence microscopy: 1. CV meteorites. Geochim Cosmochim Acta 134:100–119, doi:10.1016/j.gca.2014.02.020

Eberle AL, Mikula S, Schalek R, Lichtman J, Tate MLK, Zeidler D (2015) High-resolution, high-throughput imaging with a multibeam scanning electron microscope. J Microsc 259:114–120, doi:10.1111/jmi.12224

Finger F, Broska I, Roberts MP, Schermaier A (1998) Replacement of primary monazite by apatite-allanite-epidote coronas in an amphibolite facies granite gneiss from the Eastern Alps. Am Mineral 83:248–258, doi:10.2138/am-1998-3-408

Flowers RM, Bowring SA, Williams ML (2006a) Timescales and significance of high-pressure, high-temperature metamorphism and mafic dike anatexis, Snowbird tectonic zone, Canada. Contrib Mineral Petrol 151:558–581

Flowers RM, Mahan KH, Bowring SA, Williams ML, Pringle MS, Hodges KV (2006b) Multistage exhumation and juxtaposition of lower continental crust in the western Canadian Shield; linking high-resolution U/Pb and $^{40}Ar/^{39}Ar$ thermochronometry with pressure–temperature–deformation paths. Tectonics 25, doi:10.1029/2005TC001912

Foster G, Parrish RR, Horstwood MSA, Chenery S, Pyle J, Gibson HD (2004) The generation of prograde *P–T–t* points and paths; a textural, compositional, and chronological study of metamorphic monazite. Earth Planet Sci Lett 228:125–142

Gatewood MP, Dragovic B, Stowell HH, Baxter EF, Hirsch DM, Bloom R (2015) Evaluating chemical equilibrium in metamorphic rocks using major element and Sm–Nd isotopic age zoning in garnet, Townshend Dam, Vermont, USA. Chem Geol 401:151–168, doi:10.1016/j.chemgeo.2015.02.017

Gibson HD, Carr SD, Brown RL, Hamilton MA (2004) Correlations between chemical and age domains in monazite, and metamorphic reactions involving major pelitic phases: an integration of ID-TIMS and SHRIMP geochronology with Y–Th–U X-ray mapping. Chem Geol 211:237–260

Goldstein JI, Wood F (1966) Experimental procedures for the determination of trace elements by electron probe microanalysis. First National Electron Probe Meeting, College Park, Md

Golostnn JI (1967) Distribution of germanium inthe metallic phases of some iron-meteorites. J Geophys Res 72:4689–4696

Goncalves P, Williams ML, Jercinovic MJ (2005) Electron-microprobe age mapping of monazite. Am Mineral 90:578–587

Goodrich CA, Treiman AH, Filiberto J, Gross J, Jercinovic M (2013) K_2O-rich trapped melt in olivine in the Nakhla meteorite: Implications for petrogenesis of nakhlites and evolution of the Martian mantle. Meteorit Planet Sci 48:2371–2405, doi:10.1111/maps.12226

Gopon P, Fournelle J, Sobol PE, Llovet X (2013) Low-voltage electron-probe microanalysis of Fe–Si compounds using soft X-rays. Microsc Microanal 19:1698–1708, doi:10.1017/S1431927613012695

Grand'Homme A, Janots E, Seydoux-Guillaume A-M, Guillaume D, Bosse V, Magnin V (2016) Partial resetting of the U–Th–Pb systems in experimentally altered monazite: Nanoscale evidence of incomplete replacement. Geology 44:431–434, doi:10.1130/g37770.1

Growdon ML, Kunk MJ, Wintsch RP, Walsh GJ (2013) Telescoping metamorphic isograds; evidence from $^{40}Ar/^{39}Ar$ dating in the Orange-Mulford Belt, southern Connecticut. Am J Sci 313:1017–1053

Harlov DE, Foerster H-J (2002) High-grade fluid metasomatism on both a local and a regional scale; the Seward Peninsula, Alaska, and the Val Strona di Omegna, Ivrea-Verbano Zone, northern Italy; Part II, Phosphate mineral chemistry. J Petrol 43:801–824

Harlov DE, Hetherington CJ (2010) Partial high-grade alteration of monazite using alkali-bearing fluids: Experiment and nature. Am Mineral 95:1105–1108

Harlov DE, Wirth R, Hetherington CJ (2007) The relative stability of monazite and huttonite at 300–900ºC and 200–1000 MPa: Metasomatism and the propagation of metastable mineral phases. Am Mineral 92:1652–1664

Harlov DE, Wirth R, Hetherington CJ (2011) Fluid-mediated partial alteration in monazite: the role of coupled dissolution–reprecipitation in element redistribution and mass transfer. Contrib Mineral Petrol 162:329–348, doi:10.1007/s00410-010-0599-7

Hermann J, Rubatto D (2003) Relating zircon and monazite domains to garnet growth zones: age and duration of granulite facies metamorphism in the Val Malenco lower crust. J Metamorph Geol 21:833–852, doi:10.1046/j.1525–1314.2003.00484.x

Hetherington CJ, Jercinovic MJ, Williams ML, Mahan KH (2008) Understanding geologic processes with xenotime: Composition, chronology, and a protocol for electron probe microanalysis. Chem Geol 254:133–147

Hickmott DD, Spear FS (1992) Major- and trace-element zoning in garnets from calcareous pelites in the NW Shelburne Falls Quadrangle, Massachusetts: Garnet growth histories in retrograded rocks. J Petrol 33:965–1005

Hombourger C, Outrequin M (2013) Quantitative analysis and high resolution X-ray mapping with a field emission electron microprobe. Microsc Today 21:10–15

Janots E, Brunet F, Goffé B, Poinssot C, Burchard M, Cemič L (2007) Thermochemistry of monazite-(La) and dissakisite-(La): implications for monazite and allanite stability in metapelites. Contrib Mineral Petrol 154:1–14, doi:10.1007/s00410-006-0176-2

Janots E, Engi M, Berger A, Allaz J, Schwarz JO, Spandler C (2008) Prograde metamorphic sequence of REE minerals in pelitic rocks of the Central Alps: implications for allanite–monazite–xenotime phase relations from 250 to 610 °C. J Metamorph Geol 26:509–526, doi:10.1111/j.1525–1314.2008.00774.x

Jercinovic MJ, Williams ML (2005) Analytical perils (and progress) in electron microprobe trace element analysis applied to geochronology: Background acquisition interferences, and beam irradiation effects. Am Mineral 90:526–546

Jercinovic MJ, Williams ML, Lane ED (2008) In-situ trace element analysis of monazite and other fine-grained accessory minerals by EPMA. Chem Geol 254:197–215

Jercinovic MJ, Williams ML, Allaz J, Donovan JJ (2012) Trace analysis in EPMA. IOP Conf Ser: Mater Sci Eng 32:012012

Kelly NM, Harley SL, Möller A (2012) Complexity in the behavior and recrystallization of monazite during high-*T* metamorphism and fluid infiltration. Chem Geol 322–323:192–208, doi:10.1016/j.chemgeo.2012.07.001

Kelsey DE, Powell R (2011) Progress in linking accessory mineral growth and breakdown to major mineral evolution in metamorphic rocks: a thermodynamic approach in the Na_2O–CaO–K_2O–FeO–MgO–Al_2O_3–SiO_2–H_2O–TiO_2–ZrO_2 system. J Metamorph Geol 29:151–166, doi:10.1111/j.1525–1314.2010.00910.x

Kelsey DE, Clark C, Hand M (2008) Thermobarometric modelling of zircon and monazite growth in melt-bearing systems; examples using model metapelitic and metapsammitic granulites. J Metamorph Geol 26:199–212, doi:10.1111/j.1525–1314.2007.00757.x

Keppler H, Wyllie PJ (1990) Role of fluids in transport and fractionation of uranium and thorium in magmatic processes. Nature 348:531–533

Koenig AE (2010) Methodology for detailed trace element mapping of garnet by laser ablation ICP-MS; a look at unraveling zoning and inclusions. Abstracts with Programs–Geological Society of America 42:627–628

Kohn M (2013) Geochemical zoning in metamorphic minerals. *In*: Treatise on Geochemistry, vol 3: The Crust. Rudnick R, (ed) Elsevier, p. 249–280

Kohn MJ, Spear F (2000) Retrograde net transfer reaction insurance for pressure–temperature estimates. Geology 28:1127–1130, doi:10.1130/0091–7613(2000)28<1127:rntrif>2.0.co;2

Kohn MJ, Wieland MS, Parkinson CD, Upreti BN (2005) Five generations of monazite in Langtang gneisses; implications for chronology of the Himalayan metamorphic core. J Metamorph Geol 23:399–406

Krenn E, Finger F (2004) Metamorphic formation of Sr-apatite and Sr-bearing monazite in a high-pressure rock from the Bohemian Massif. Am Mineral 89:1323–1329

Kylander–Clark ARC (2017) Petrochronology by laser–ablation inductively coupled plasma mass spectrometry. Rev Mineral Geochem 83:183–198

Kylander-Clark ARC, Hacker BR, Cottle JM (2013) Laser-ablation split-stream ICP petrochronology. Chem Geol 345:99–112, doi:10.1016/j.chemgeo.2013.02.019

Lanari P, Engi M (2017) Local bulk composition effects on metamorphic mineral assemblages. Rev Mineral Geochem 83:55–102

Lanari P, Rolland Y, Schwartz S, Vidal O, Guillot S, Tricart P, Dumont T (2014) *P–T–t* estimation of deformation in low-grade quartz–feldspar-bearing rocks using thermodynamic modelling and $^{40}Ar/^{39}Ar$ dating techniques: example of the Plan-de-Phasy shear zone unit (Briançonnais Zone, Western Alps). Terra Nova 26:130–138, doi:10.1111/ter.12079

Larson KP, Cottle JM, Godin L (2011) Petrochronologic record of metamorphism and melting in the upper Greater Himalayan sequence, Manaslu–Himal Chuli Himalaya, west-central Nepal. Lithosphere 3:379–392, doi:10.1130/l149.1

Lifshin E, Doganaksoy N, Sirois J, Gauvin R (1999) Statistical considerations in microanalysis by energy-dispersive spectrometry. Microsc Microanal 4:598–604

MacRae CM, Wilson NC, Torpy A, Bergmann J, Takahashi H (2016a) Holistic mapping—first results combining SXES, Windowless-SDD and CL spectrometry in an EPMA. MAS EPMA 2016 Topical Conference Program Guide with Abstracts 82–83

MacRae CM, Wilson NC, Torpy A, Bergmann J, Takahashi H (2016b) Collecting and analyzing 1.6 eV–20 keV emission spectra in an EPMA. Microsc Microanal 22 (Suppl 3):410–411

MacRae CM, Torpy A, Glenn AM, Pownceby MI, Grey IE, Wilson NC, Pundas P (2016c) Zircon zonation and trace chemistry characterized by mapping and analysis. MAS EPMA 2016 Topical Conference Program Guide with Abstracts 110–111

Mahan KH, Goncalves P, Williams ML, Jercinovic MJ (2006) Dating metamorphic reactions and fluid flow: application to exhumation of high-*P* granulites in a crustal-scale shear zone, western Canadian Shield. J Metamorph Geol 24:193–217

McFarlane CRM, Connelly JN, Carlson WD (2005) Monazite and xenotime petrogenesis in the contact aureole of the Makhavinekh Lake Pluton, northern Labrador. Contrib Mineral Petrol 148:524–541

McSwiggen P, Mori N, Takakura M, Nielsen C (2011) Improving analytical spatial resolution with the JEOL field emission electron microprobe. Microsc Microanal 17 (Suppl 2):624–625

Merlet C, Bodinier J-L (1990) Electron microprobe determination of minor and trace transition elements in silicate minerals: A method and its application to mineral zoning in the peridotite nodule PHN 1611. Chem Geol 83:55–69, doi:10.1016/0009–2541(90)90140–3

Montel J, Foret S, Veschambre M, Nicollet C, Provost A (1996) Electron microprobe dating of monazite. Chem Geol 131:37–53

Moran K, Wuhrer R (2016) Current state of combined EDS–WDS quantitative X-ray mapping. Microsc Microanal 22 (Suppl 3):92–93

Muhling JR, Fletcher IR, Rasmussen B (2012) Dating fluid flow and Mississippi Valley type base-metal mineralization in the Paleoproterozoic Earaheedy Basin, Western Australia. Precambrian Res 212–213:75–90, doi:10.1016/j.precamres.2012.04.016

Müller W, Kelley SP, Villa IM (2002) Dating fault-generated pseudotachylytes: comparison of $^{40}Ar/^{39}Ar$ stepwise-heating, laser-ablation and Rb–Sr microsampling analyses. Contrib Mineral Petrol 144:57–77, doi:10.1007/s00410-002-0381-6

Overstreet WC (1967) The geologic occurrence of monazite. U S Geological Survey Professional Paper

Park JB, Kim YJ, Kim SM, Yoo JM, Kim Y, Gorbachev R, Barbolina II, Kim SJ, Kang S, Yoon MH, Cho SP (2016) Non-destructive electron microscopy imaging and analysis of biological samples with graphene coating. 2D Mater 3:045004

Parrish RR (1990) U–Pb dating of monazite and its application to geological problems. Can J Earth Sci 27:1431–1450, doi:10.1139/e90-152

Parslow GR, Brandstatter F, Kurat G, Thomas D (1985) Chemical ages and mobility of U and Th in anatectites of the Cree Lake Zone, Saskatchewan. Can Mineral 23:543–551

Peterman EM, Snoeyenbos DR, Jercinovic MJ, Kylander-Clark A (2016) Dissolution–reprecipitation metasomatism and growth of zircon within phosphatic garnet in metapelites from western Massachusetts. Am Mineral 101:1792–1806, doi:10.2138/am-2016-5524

Pyle JM, Spear FS (1999) Yttrium zoning in garnet: coupling of major and accessory phases during metamorphic reactions. Geol Mater Res 1:1–49

Pyle JM, Spear FS (2003) Four generations of accessory-phase growth in low-pressure migmatites from SW New Hampshire. Am Mineral 88:338–351

Pyle JM, Spear FS, Wark DA (2002) Electron microprobe analysis of REE in apatite, monazite and xenotime; protocols and pitfalls. Rev Mineral Geochem 48:337–362

Pyle JM, Spear FS, Wark DA, Daniel CG, Storm LC (2005) Contributions to precision and accuracy of monazite microprobe ages. Am Mineral 90:547–577, doi:10.2138/am.2005.1340

Rapp RP, Ryerson FJ, Miller CF (1987) Experimental evidence bearing on the stability of monazite during crustal anaatexis. Geophys Res Lett 14:307–310, doi:10.1029/GL014i003p00307

Rasmussen B (1996) Early-diagenetic REE-phosphate minerals (florencite, gorceixite, crandallite, and xenotime) in marine sandstones; a major sink for oceanic phosphorus. Am J Sci 296:601–632, doi:10.2475/ajs.296.6.601

Rasmussen B, Muhling JR (2007) Monazite begets monazite: evidence for dissolution of detrital monazite and reprecipitation of syntectonic monazite during low-grade regional metamorphism. Contrib Mineral Petrol 154:675–689, doi:10.1007/s00410-007-0216-6

Rasmussen B, Muhling JR (2009) Reactions destroying detrital monazite in greenschist-facies sandstones from the Witwatersrand basin, South Africa. {Stepanov, 2012 #1783}Chem Geol 264:311–327, doi:10.1016/j.chemgeo.2009.03.017

Rasmussen B, Sheppard S, Fletcher IR (2006) Testing ore deposit models using in situ U–Pb geochronology of hydrothermal monazite: Paleoproterozoic gold mineralization in northern Australia. Geology 34:77–80, doi:10.1130/g22058.1

Rasmussen B, Fletcher IR, Muhling JR (2007) In situ U–Pb dating and element mapping of three generations of monazite: Unravelling cryptic tectonothermal events in low-grade terranes. Geochim Cosmochim Acta 71:670–690, doi:10.1016/j.gca.2006.10.020

Reed SJB (1993) Electron Microprobe Analysis. Cambridge University Press, Cambridge
Regis D, Warren CJ, Mottram CM, Roberts NMW (2016) Using monazite and zircon petrochronology to constrain the *P–T–t* evolution of the middle crust in the Bhutan Himalaya. J Metamorph Geol 34:617–639, doi:10.1111/jmg.12196
Robertson VE, McSwiggen P (2016) Low Voltage, high spatial resolution, field emission SEM imaging coupled with new low energy X-ray spectrometers, a novel new technique—successes and challenges. MAS EPMA 2016 Topical Conference Program Guide with Abstracts:86–87
Rocha BC, Moraes R, Moller A, Cioffi CR, Jercinovic MJ (2017) Timing of anataxis and melt crystallization in the Socorro-Guaxupe Nappe, SE Brazil: Insights from trace element composition of zircon, monazite, and garnet coupled to U–Pb geochronology. Lithos 277:337–355, doi: 10.1016/j.lithos.2016.05.020
Rubatto D, Hermann J (2007) Experimental zircon/melt and zircon/garnet trace element partitioning and implications for the geochronology of crustal rocks. Chem Geol 241:38–61, doi:10.1016/j.chemgeo.2007.01.027
Rubatto D, Hermann J, Buick IS (2006) Temperature and bulk composition control on the growth of monazite and zircon during low-pressure anatexis (Mount Stafford, central Australia). J Petrol 47:1973–1996
Ruiz-Agudo E, Putnis CV, Putnis A (2014) Coupled dissolution and precipitation at mineral–fluid interfaces. Chem Geol 383:132–146, doi:10.1016/j.chemgeo.2014.06.007
Scherrer NC, Engi M, Gnos E, Jakob V, Liechti A (2000) Monazite analysis; from sample preparation to microprobe age dating and REE quantification. Schweiz Mineral Petrogr Mitt 80:93–105
Schoene B, Baxter EF (2017) Petrochronology and TIMS. Rev Mineral Geochem 83:231–260
Schneider S, Hammerschmidt K, Rosenberg CL (2013) Dating the longevity of ductile shear zones: Insight from $^{40}Ar/^{39}Ar$ in situ analyses. Earth Planet Sci Lett 369–370:43–58, doi:10.1016/j.epsl.2013.03.002
Seydoux-Guillaume A-M, Montel J-M, Bingen B, Bosse V, de Parseval P, Paquette J-L, Janots E, Wirth R (2012) Low-temperature alteration of monazite: Fluid mediated coupled dissolution–precipitation, irradiation damage, and disturbance of the U–Pb and Th–Pb chronometers. Chem Geol 330–331:140–158, doi:10.1016/j.chemgeo.2012.07.031
Spear FS (2010) Monazite-allanite phase relations in metapelites. Chem Geol 279:55–62, doi:10.1016/j.chemgeo.2010.10.004
Spear FS, Kohn MJ (1996) Trace element zoning in garnet as a monitor of crustal melting. Geology 24:1099–1102
Spear FS, Pyle JM (2002) Apatite, monazite, and xenotime in metamorphic rocks. Rev Mineral Geochem 48:293–335
Spear FS, Pyle JM (2010) Theoretical modeling of monazite growth in a low Ca metapelite. Chem Geol 273:111–119, doi:10.1016/j.chemgeo.2010.02.016
Spear FS, Pyle JM, Cherniak D (2009) Limitations of chemical dating of monazite. Chem Geol 266:218–230, doi:10.1016/j.chemgeo.2009.06.007
Stepanov AS, Hermann J, Rubatto D, Rapp RP (2012) Experimental study of monazite/melt partitioning with implications for the REE, Th and U geochemistry of crustal rocks. Chem Geol 300–301:200–220, doi:10.1016/j.chemgeo.2012.01.007
Susan D, Grant RP, Rodelas JM, Michael JR, Maguire MC (2015) Comparing field emission electron microprobe to traditional EPMA for analysis of metallurgical specimens. Microsc Microanal 21 (Suppl 3):2107–2108
Suzuki K, Adachi M (1991) Precambrian provenance and Silurian metamorphism of the Tsunosawa paragneiss in the South Kitakami terrane, Northeast Japan, revealed by the chemical Th–U–total Pb isochron ages of monazite, zircon and xenotime. J Geochem 25:357–376
Terauchi M, Takahashi H, Handa N, Murano T, Koike M, Kawachi T, Imazono T, Koeda M, Nagano T, Sasai H, Oue Y (2012) Ultrasoft X-ray emission spectroscopy using a newly designed wavelength-dispersive spectrometer attached to a transmission electron microscope. J Electron Microsc 61:1–8
Tracy RJ (1982) Compositional zoning and inclusions in metamorphic minerals. Rev Mineral 10:355–397
Ubide T, McKenna CA, Chew DM, Kamber BS (2015) High-resolution LA-ICP-MS trace element mapping of igneous minerals; in search of magma histories. Chem Geol 409:157–168, doi:10.1016/j.chemgeo.2015.05.020
Vallini D, Rasmussen B, Krapež B, Fletcher IR, McNaughton NJ (2002) Obtaining diagenetic ages from metamorphosed sedimentary rocks: U–Pb dating of unusually coarse xenotime cement in phosphatic sandstone. Geology 30:1083–1086, doi:10.1130/0091–7613(2002)030<1083:odafms>2.0.co;2
Vance D, Müller W, Villa IM (eds) (2003) Geochronology: linking the isotope record with petrology and textures
Villa IM (2016) Diffusion in mineral geochronometers: Present and absent. Chem Geol 420:1–10, doi:10.1016/j.chemgeo.2015.11.001
Villa IM, Williams ML (2012) Geochronology of metasomatic events. *In*:Metasomatism and the Chemical Transformation of Rock. Harlov DE, Austrheim H (eds). Springer-Verlag, Heidelberg, p. 171–202
Villa IM, Hermann J, Müntener O, Trommsdorff V (2000) $^{39}Ar–^{40}Ar$ dating of multiply zoned amphibole generations (Malenco, Italian Alps). Contrib Mineral Petrol 140:363–381, doi:10.1007/s004100000197
Villa IM, Bucher S, Bousquet R, Kleinhanns IC, Schmid SM (2014) Dating polygenetic metamorphic assemblages along a transect across the Western Alps. J Petrol 55:803–830, doi:10.1093/petrology/egu007

Villaseca C, Martín Romera C, De la Rosa J, Barbero L (2003) Residence and redistribution of REE, Y, Zr, Th and U during granulite-facies metamorphism: behaviour of accessory and major phases in peraluminous granulites of central Spain. Chem Geol 200:293–323, doi:10.1016/S0009-2541(03)00200–6

Wells ML, Spell TL, Hoisch TD, Arriola T, Zanetti KA (2008) Laser-probe $^{40}Ar/^{39}Ar$ dating of strain fringes: Mid-Cretaceous synconvergent orogen-parallel extension in the interior of the Sevier orogen. Tectonics 27: TC3012, doi:10.1029/2007TC002153. doi:10.1029/2007TC002153

Wendt I, Carl C (1991) The statistical distribution of the mean squared weighted deviation. Chem Geol; Isotope Geosci Sect 86:275–285

White AP, Hodges KV (2003) Pressure–temperature–time evolution of the Central East Greenland Caledonides: quantitative constraints on crustal thickening and synorogenic extension. J Metamorph Geol 21:875–897, doi:10.1046/j.1525–1314.2003.00489.x

Whitney DL, Evans BW (2010) Abbreviations for names of rock-forming minerals. Am Mineral 95:185–187, doi:10.2138/am.2010.3371

Williams ML, Jercinovic MJ (2012) Tectonic Interpretation of metamorphic tectonites: integrating compositional mapping, microstructural analysis, and in-situ monazite dating. J Metamorph Geol 30:739–732, doi:10.1111/j.1525–1314.2012.00995.x

Williams ML, Jercinovic MJ, Terry M (1999) High resolution "age" mapping, chemical analysis, and chemical dating of monazite using the electron microprobe: A new tool for tectonic analysis. Geology 27:1023–1026

Williams ML, Jercinovic MJ, Goncalves P, Mahan KH (2006) Format and philosophy for collecting, compiling, and reporting microprobe monazite ages. Chem Geol 225:1–15

Williams ML, Jercinovic MJ, Hetherington CJ (2007) Microprobe monazite geochronology: understanding geologic processes by integrating composition and chronology. Ann Rev Earth Planet Sci 35:137–175

Williams ML, Jercinovic MJ, Harlov DE, Budzyn B, Hetherington CJ (2011) Resetting monazite ages during fluid-related alteration. Chem Geol 283:218–225, doi:10.1016/j.chemgeo.2011.01.019

Wing BA, Ferry JM, Harrison TM (2003) Prograde destruction and formation of monazite and allanite during contact and regional metamorphism of pelites; petrology and geochronology. Contrib Mineral Petrol 145:228–250

Wintsch RP, Aleinikoff JN, Yi K (2005) Foliation development and reaction softening by dissolution and precipitation in the transformation of granodiorite to orthogneiss, Glastonbury Complex, Connecticut, U.S.A. Can Mineral 43:327–347, doi:10.2113/gscanmin.43.1.327

Wong MS, Williams ML, McLelland JM, Jercinovik MJ, Kowalkoski J (2012) Late Ottawan extension in the eastern Adirondack Highlands: Evidence from structural studies and zircon and monazite geochronology. Geol Soc Am Bull 124:857–869, doi:10.1130/b30481.1

Xing L, Trail D, Watson EB (2013) Th and U partitioning between monazite and felsic melt. Chem Geol 358:46–53, doi:10.1016/j.chemgeo.2013.07.009

Yang P, Pattison D (2006) Genesis of monazite and Y zoning in garnet from the Black Hills, South Dakota. Lithos 88:233–253, doi:10.1016/j.lithos.2005.08.012

Yang P, Rivers T, Jackson SJ (1999) Crystal-chemical and thermal controls on trace-element partitioning between coexisting garnet and biotite in metamorphic rocks from western Labrador. Can Mineral 37:443–468

Zi J-W, Rasmussen B, Muhling JR, Fletcher IR, Thorne AM, Johnson SP, Cutten HN, Dunkley DJ, Korhonen FJ (2015) In situ U–Pb geochronology of xenotime and monazite from the Abra polymetallic deposit in the Capricorn Orogen, Australia: Dating hydrothermal mineralization and fluid flow in a long-lived crustal structure. Precambrian Res 260:91–112, doi:10.1016/j.precamres.2015.01.010

Ziebold TO (1967) Precision and sensitivity in electron microprobe analysis. Anal Chem 36:858–861